

1 Dynamics of human protein kinase Aurora A linked to drug selectivity

2
3
4 Warintra Pitsawong^{*,a}, Vanessa Buosi^{*,a}, Renee Otten^{*,a}, Roman V. Agafonov^{*,a} Adelajda Zorba^a,
5 Nadja Kern^a, Steffen Kutter^a, Gunther Kern^a, Ricardo A. P. Pádua^a, Xavier Meniche^b, and
6 Dorothee Kern^{#,a}

7
8 ^a*Department of Biochemistry and Howard Hughes Medical Institute, Brandeis University,*
9 *Waltham, MA 02452, USA*

10 ^b*Department of Microbiology and Physiological Systems, University of Massachusetts Medical*
11 *School, Worcester, MA 01605, USA*

12 *these authors contributed equally to this work

13 #corresponding author

14 15 **Abstract**

16 Protein kinases are major drug targets, but the development of highly-selective inhibitors has
17 been challenging due to the similarity of their active sites. The observation of distinct structural
18 states of the fully-conserved Asp-Phe-Gly (DFG) loop has put the concept of conformational
19 selection for the DFG-state at the center of kinase drug discovery. Recently, it was shown that
20 Gleevec selectivity for the Tyr-kinases Abl was instead rooted in conformational changes after
21 drug binding. Here, we investigate whether protein dynamics after binding is a more general
22 paradigm for drug selectivity by characterizing the binding of several approved drugs to the
23 Ser/Thr-kinase Aurora A. Using a combination of biophysical techniques, we propose a
24 universal drug-binding mechanism, that rationalizes selectivity, affinity and long on-target
25 residence time for kinase inhibitors. These new concepts, where protein dynamics in the drug-
26 bound state plays the crucial role, can be applied to inhibitor design of targets outside the
27 kinome.

28 29 **eLife digest**

30 The Ser/Thr kinase Aurora A is an important target for the development of new anticancer
31 therapies. A longstanding question is how to specifically and effectively inhibit only this kinase in
32 a background of over 550 protein kinases with very similar structures. To this end,
33 understanding the inhibition mechanism of Aurora A by different drugs is essential. Here, we
34 characterize the kinetic mechanism of three distinct kinase drugs, Gleevec (Imatinib),
35 Danusertib (PHA739358) and AT9283 (Pyrazol-4-yl Urea) for Aurora A. We show that inhibitor
36 affinities do not rely exclusively on the recognition of a specific conformation of the Asp-Phe-Gly

37 loop of the kinase. Our quantitative kinetics data put forward an opposing mechanism in which a
38 slow conformational change after drug binding (i.e., induced-fit step) dictates drug affinity.

39

40 **Introduction**

41 Protein kinases have become the number one drug target of the 21th century (Cohen, 2002;
42 Hopkins & Groom, 2002), due to their central role in cellular processes and involvement in
43 various types of cancer (Carvajal, Tse, & Schwartz, 2006; Gautschi et al., 2008; Katayama &
44 Sen, 2010). Despite their therapeutic significance, the development of specific kinase inhibitors
45 proves to be extremely challenging because they must discriminate between the very similar
46 active sites of a large number of kinases in human cells. One of the biggest success stories is
47 Gleevec: a highly selective drug that specifically targets Abl kinase, providing an efficient
48 treatment of chronic myelogenous leukemia (CML) and minimizing side effects (Iqbal & Iqbal,
49 2014). Despite being a multi-billion-dollar cancer drug, the mechanism responsible for its
50 impressive selectivity has been elusive until recently. Seminal work by the Kuriyan lab
51 demonstrated that Gleevec can only bind to an inactive DFG (for Asp-Phe-Gly) loop
52 conformation in the “out-conformation” due to steric clash of the active, DFG-in conformation
53 (Nagar et al., 2002; Schindler et al., 2000; Seeliger et al., 2007). Since then it has long been
54 proposed that the conformational state of the fully conserved DFG loop (Taylor, Keshwani,
55 Steichen, & Kornev, 2012) dictates the selectivity for Gleevec and other kinase inhibitors
56 (Lovera et al., 2012; Nagar et al., 2002; Schindler et al., 2000; Treiber & Shah, 2013; Xu,
57 Harrison, & Eck, 1997). The orientation of the DFG-motif and its possible steric clashes is
58 indeed important for the ability of a class of inhibitors to bind to the kinase, but proved
59 insufficient to explain drug selectivity and affinity. Earlier elegant work on Src and Abl
60 recognized this and explored other hypotheses (e.g., differences in drug-binding pocket,
61 energetic changes remote from the binding site and a conformational-selection mechanism) to
62 reconcile the differences in Gleevec binding (Dar, Lopez, & Shokat, 2008; Levinson et al., 2006;
63 Seeliger et al., 2007; Seeliger et al., 2009), but without conclusive success. Recent quantitative
64 binding kinetics combined with ancestral sequence reconstruction put forward a mechanism
65 where an induced-fit step after drug binding is the key determinant for Gleevec’s selectivity
66 (Agafonov, Wilson, Otten, Buosi, & Kern, 2014; Wilson et al., 2015), and fully recapitulates the
67 binding affinities.

68 Here we ask the question whether this fundamentally different mechanism is a more
69 general principle for drug efficacy and selectivity not only for Tyr kinases such as Abl, but also
70 for Ser/Thr kinases. To this end, we chose the Ser/Thr kinase Aurora A and investigated the

71 binding kinetics of three distinct kinase drugs: Danusertib, AT9283, and Gleevec. Aurora A
72 kinase is one of the key regulators of mitotic events, including mitotic entry, centrosome
73 maturation and spindle formation (Fu, Bian, Jiang, & Zhang, 2007; Lukasiewicz & Lingle, 2009;
74 Marumoto, Zhang, & Saya, 2005), as well as assisting in neuronal migration (Nikonova,
75 Astsaturov, Serebriiskii, Dunbrack, & Golemis, 2013). Aurora A has attracted significant
76 attention for the development of targeted agents for cancer because it is overexpressed in a
77 wide range of tumors, including breast, colon, ovary and skin malignancies (Carvajal et al.,
78 2006; Gautschi et al., 2008; Katayama & Sen, 2010; Lok, Klein, & Saif, 2010; Marzo & Naval,
79 2013). The focus was mainly on ATP-competitive inhibitors, but more recently inhibition by
80 allosteric compounds has also been pursued with the aim of achieving higher selectivity (Asteriti
81 et al., 2017; Bayliss, Burgess, & McIntyre, 2017; Burgess et al., 2016; Janecek et al., 2016;
82 McIntyre et al., 2017). So far, only the clinical significance of Aurora A inhibition by ATP-
83 competitive drugs has been established (Bavetsias & Linardopoulos, 2015; Borisa & Bhatt,
84 2017), but little is known about their binding mechanisms. Many high-resolution X-ray structures
85 of Aurora A kinase bound to different inhibitors have been solved (Bavetsias et al., 2015;
86 Dodson et al., 2010; Fancelli et al., 2006; Ferguson et al., 2017; Heron et al., 2006; Howard et
87 al., 2009; Kilchmann et al., 2016; Martin et al., 2012; Zhao et al., 2008), but the selectivity profile
88 of those kinase inhibitors remains very difficult to explain.

89 The drugs used in this study are small, ATP-competitive inhibitors. Danusertib
90 (PHA739358) and AT9283 were developed for Aurora kinases, whereas Gleevec is selective for
91 the Tyr kinase Abl. Danusertib inhibits all members of the Aurora family with low nanomolar IC_{50}
92 values (13, 79 and 61 nM for Aurora A, B and C, respectively) (Carpinelli et al., 2007; Fraedrich
93 et al., 2012) and was one of the first Aurora kinase inhibitors to enter phase I and II clinical trials
94 (Kollareddy et al., 2012; Steeghs et al., 2009). A crystal structure of Danusertib bound to Aurora
95 A kinase shows an inactive kinase with the DFG-loop in the *out* conformation (Fancelli et al.,
96 2006). AT9283 inhibits both Aurora A and B with an IC_{50} of 3 nM (Howard et al., 2009) and has
97 also entered several clinical trials (Borisa & Bhatt, 2017). Interestingly, the crystal structure of
98 Aurora A with AT9283 shows that this drug binds to the DFG-*in*, active conformation of the
99 kinase (Howard et al., 2009). Both drugs are high-affinity binders that reportedly bind to a
100 discrete kinase conformation and would allow us to probe for a conformational-selection step.
101 Lastly, we selected Gleevec as a drug that is not selective for Aurora A and should, therefore,
102 have a weaker binding affinity. We reasoned that this choice of inhibitors could reveal general
103 mechanisms underlying drug selectivity and affinity.

104 The combination of X-ray crystallography, NMR spectroscopy and comprehensive
105 analysis of drug binding and release kinetics delivered a general mechanistic view. Differential
106 drug affinity is not rooted in the overwhelmingly favored paradigm of the DFG-conformation, but
107 instead in the dynamic personality of the kinase that is manifested in conformational changes
108 after drug binding. Notably, such conformational changes have evolved for its natural
109 substrates, and the drugs take advantage of this built-in protein dynamics.

110

111 **Results**

112 **Dephosphorylated Aurora A samples both an inactive and active structure**

113 A plethora of X-ray structures and functional assays led to the general notion that
114 dephosphorylated Aurora A and, more universally, Ser/Thr kinases are in an inactive
115 conformation and that phosphorylation or activator binding induces the active structure. A
116 comparison of many X-ray structures of inactive and active forms of Ser/Thr kinases resulted in
117 an elegant proposal of the structural hallmarks for the active state by Taylor and collaborators:
118 the completion of both the regulatory and catalytic spines spanning the N- and C-terminal
119 domains, including the orientation of the DFG-motif (Kornev & Taylor, 2010, 2015). X-ray
120 structures, however, provide merely static snapshots of possible kinase conformations that do
121 not necessarily reflect the situation in solution. In fact, recent experimental data postulate that
122 phosphorylation of Aurora A does not “lock” the kinase in the active conformation, and that the
123 activation-loop still exhibits conformational dynamics (Gilburt et al., 2017; Ruff et al., 2018). On
124 the other hand, X-ray crystallography provides high-resolution structural data that cannot readily
125 be obtained from FRET or EPR and IR spectroscopy.

126 Two crystals from the same crystallization well capture both the inactive and active
127 conformations of dephosphorylated Aurora A bound with AMPPCP (Figure 1A, B). As
128 anticipated, the first structure (PDB 4C3R (Zorba et al., 2014)) superimposes with the well-
129 known inactive, dephosphorylated Aurora A structure (PDB 1MUO (Cheetham et al., 2002)) and
130 the activation loop is not visible as commonly observed for kinases lacking phosphorylation of
131 the activation loop (Zorba et al., 2014). The second structure (PDB 6CPF; Table 1) adopts the
132 same conformation as the previously published phosphorylated, active structure (PDB 1OL7
133 (Bayliss, Sardon, Vernos, & Conti, 2003)) (Figure 1C) and the first part of the activation loop
134 could be built, although the B-factors are high. Every hallmark of an active state is seen for this
135 dephosphorylated protein, including the DFG-*in* conformation that is essential for completing the
136 regulatory spine. In contrast, the DFG-loop is in the *out* position for the inactive form of Aurora A
137 (Figure 1D, cyan). In the active, non-phosphorylated structure, electron density is seen in the

138 canonical tighter Mg²⁺-binding site, where the metal ion is coordinated to the α- and β-
139 phosphates of AMPPCP and Asp274. The presence of the metal is supported by the
140 CheckMyMetal (Zheng et al., 2017) validation, except that the coordination is incomplete. We
141 surmise that two water molecules, not visible in our data, complete the coordination sphere as is
142 seen in several higher-resolution structures. In the inactive structure, no electron density for
143 Mg²⁺ can be identified possibly due to the fact that Asp274 is rotated to the DFG-*out* position
144 and is, therefore, lost as coordination partner. Furthermore, sampling of the active conformation
145 does not depend on AMPPCP binding as dephosphorylated, apo Aurora A also crystallizes in
146 the active form (PDB 6CPE; Figure 1E, F and Table 1). Our results are consistent with other
147 crystallographic studies on wild-type, dephosphorylated Aurora A in its apo or nucleotide bound
148 state, where the kinase was also found in the active conformation (Gustafson et al., 2014;
149 Janecek et al., 2016; Nowakowski et al., 2002).

150 We note that in Aurora kinase sequences a tryptophan residue, Trp277, is immediately
151 following the DFG motif and displays a drastically different orientation whether Aurora A is in an
152 active (DFG-*in*) or inactive (DFG-*out*) conformation (Figure 1D). This Trp moiety is unique for
153 the Aurora kinase family in the Ser/Thr kinome and its position is suggested to be important for
154 tuning the substrate specificity (C. Chen et al., 2014). We used this Trp residue as probe to
155 monitor the DFG flip and drug binding in real time as described below.

156 The fact that the inactive and active states are seen in the crystal implies that both are
157 sampled; however, it does not deliver information about the relative populations or
158 interconversion rates. Therefore, we set out to monitor the conformational exchange of the
159 DFG-*in/out* flip in solution. “Owing to the reported importance of the DFG flip for activity,
160 regulation and drug design, there have been extensive efforts to characterize this
161 conformational equilibrium by computation (Badrinarayan & Sastry, 2014; Barakat et al., 2013;
162 Meng, Lin, & Roux, 2015; Meng, Pond, & Roux, 2017; Sarvagalla & Coumar, 2015; Shukla,
163 Meng, Roux, & Pande, 2014). The general notion of these computational studies is that in the
164 absence of phosphorylation the inactive form of the kinase is most favored, in agreement with
165 experimental evidence. Nevertheless, short-lived excursions to the active state are observed.

166 As an experimental approach, NMR spectroscopy is an obvious choice; however efforts on
167 several Ser/Thr and Tyr kinases led to the general conclusion that the activation loop, including
168 the DFG motif and most of the active-site residues, cannot be detected due to exchange
169 broadening, and at best can only be seen after binding of drugs that stabilize conformations
170 (Campos-Olivas, Marenchino, Scapozza, & Gervasio, 2011; Langer et al., 2004; Vajpai et al.,
171 2008; Vogtherr et al., 2006).

172 $[^1\text{H}-^{15}\text{N}]$ -HSQC experiments on uniformly ^{15}N -labeled samples of Aurora A proved to be
173 no exception: many peaks are missing and only three out of four tryptophan side chain indole
174 signals are seen in the 2D spectra of a $[^{15}\text{N}]$ -Trp labeled sample (Figure 2A, B). Therefore, we
175 sought a strategy to overcome this general problem of exchange broadening that hampers the
176 detection of the DFG equilibrium. Aurora A was produced containing 5-fluoro-tryptophan
177 residues to allow for one-dimensional ^{19}F spectroscopy to deal with exchange broadening while
178 providing sensitivity close to proton NMR (Kitevski-LeBlanc & Prosser, 2012). Now, we observe
179 as expected four peaks in our NMR spectra for apo- and AMPPCP-bound wild-type Aurora A
180 (Figure 2C). A deconvolution of the spectrum yields almost identical integral values for all four
181 peaks, whereas the linewidth of one resonance is approximately 5-fold larger (Figure 2D, purple
182 signal). This broad peak is a prime candidate to originate from Trp277, directly adjacent to the
183 DFG-loop. The W277L mutation confirmed our hypothesis (Figure 2C), and the extensive line
184 broadening of this signal in a one-dimensional spectrum is consistent with its absence in the
185 $[^1\text{H},^{15}\text{N}]$ -HSQC spectrum. Of note, the W277L mutant is still active, as confirmed by a kinase
186 assay, most likely because this Trp is not conserved in Ser/Thr kinases, where a Leu residue is
187 found at the position for several Ser/Thr family members. Mutating any of the other, more
188 conserved Trp residues resulted in insoluble proteins. The broad line shape for the Trp277 peak
189 hints at severe exchange broadening in the surrounding of the DFG-loop and is consistent with
190 the high B-factors for Trp277 and its neighboring residues observed in all crystal structures
191 described here. Determination of relative populations and rate constants of interconversion is
192 not possible from this data, but this missing piece of information was obtained by stopped-flow
193 kinetics of drug binding.

194

195 **Gleevec binding to Aurora A distinguishes conformational selection versus induced-fit** 196 **mechanisms**

197 Through groundbreaking experiments on the Tyr kinases Abl and Src, the concept of drug
198 selectivity based on the DFG-loop conformation has received considerable attention in kinase
199 drug discovery (Lovera et al., 2012; Treiber & Shah, 2013). A recent report provides kinetic
200 evidence for such conformational selection, but identifies an induced-fit step after drug binding
201 as the overwhelming contribution for Gleevec selectivity towards Abl compared to Src
202 (Agafonov et al., 2014). Here, we ask the obvious question if this mechanism of Gleevec binding
203 to Abl might exemplify a more general mechanism for kinase inhibitors.

204 To assess which kinetic steps control drug affinity and selectivity, we first studied the
205 binding kinetics for Gleevec to Aurora A by stopped-flow spectroscopy using intrinsic tryptophan

206 fluorescence under degassing conditions to reduce photobleaching. At 25 °C, the binding of
207 Gleevec to Aurora A was too fast to be monitored and, therefore, experiments were performed
208 at 10 °C. Binding kinetics of Gleevec to Aurora A exhibited biphasic kinetic traces (Figure 3A).
209 The first, fast phase is characterized by a decrease in the fluorescence intensity (Figure 3A, B),
210 with an observed rate constant, k_{obs} , increasing linearly with Gleevec concentration (Figure 3C).
211 The slope corresponds to the bimolecular rate constant, $k_2 = (1.1 \pm 0.3) \times 10^6 \text{ M}^{-1}\text{s}^{-1}$, of Gleevec
212 binding to Aurora A and the dissociation of Gleevec is determined from the intercept, $k_{-2} = 31 \pm$
213 2 s^{-1} (Figure 3C). We note that the parameters for the physical binding step are comparable to
214 the ones obtained for Gleevec binding to Abl (*cf.* $k_2 = (1.5 \pm 0.1) \times 10^6 \text{ M}^{-1}\text{s}^{-1}$ and $k_{-2} = 25 \pm 6 \text{ s}^{-1}$,
215 measured at 5 °C) (Agafonov et al., 2014). The second, slow phase exhibits an increase in
216 fluorescence intensity (Figure 3A), with the observed rate constant decreasing with Gleevec
217 concentration (Figure 3D). The decreasing k_{obs} provides unequivocal evidence of
218 conformational selection, where its rate of interconversion is slower than the rate of ligand
219 dissociation ($k_1 + k_{-1} \ll k_{-2}$). The values of k_1 and k_{-1} can be estimated by fitting the data to
220 Equation 1 and are $0.014 \pm 0.001 \text{ s}^{-1}$ and $0.011 \pm 0.002 \text{ s}^{-1}$, respectively (Figure 3D). These rate
221 constants represent the conformational change from DFG-*in* to -*out* and vice versa since
222 Gleevec is a DFG-*out* selective inhibitor due to steric hindrance (Nagar et al., 2002; Schindler et
223 al., 2000; Seeliger et al., 2007).

224 In order to more rigorously analyze the data and test the model, all time courses of the
225 fluorescence changes were globally fit using the microscopic rate constants determined above
226 as starting values (Figure 4) to the model in Figure 3G, where also the resulting microscopic
227 rate constants are given. The lack of a conformational transition after drug binding (i.e., induced-
228 fit step) in Aurora A should dramatically decrease drug affinity in comparison to Abl. Indeed,
229 Gleevec binds to Aurora A with a K_D of $24 \pm 7 \mu\text{M}$ (Figure 3F) compared to the low nM affinity to
230 Abl (Agafonov et al., 2014). Two pieces of independent evidence establish that there is indeed
231 no induced-fit step in Gleevec binding to Aurora A: (i) the calculated K_D from the kinetic scheme
232 is in agreement with the macroscopically measured K_D (*cf.* Figure 3G and 3F), and (ii) the
233 observed k_{off} from the dilution experiment (Figure 3E) coincides with the physical dissociation
234 rate (i.e., intercept of the binding plot, $31 \pm 2 \text{ s}^{-1}$, in Figure 3C). In summary, the lack of an
235 induced-fit step for Gleevec binding to Aurora A is the major reason for Gleevec's weak binding,
236 and not the DFG-loop conformation or physical drug-binding step, consistent with our earlier
237 results (Wilson et al., 2015).

238

239 **Kinetics of Danusertib binding to Aurora A: three-step kinetics with conformational**
240 **selection and an induced-fit step**

241 Next, we wanted to shed light on why Danusertib, unlike Gleevec, binds very tightly to Aurora A.
242 A high-resolution X-ray structure shows Danusertib bound to Aurora A's active site with its DFG-
243 loop in the *out* conformation (Figure 5A) (Fancelli et al., 2006), and to rationalize Danusertib's
244 high affinity we measured the kinetics of Danusertib binding to Aurora A directly by stopped-flow
245 experiments at 25 °C. An increase in fluorescence intensity was observed at all Danusertib
246 concentrations and showed double-exponential behavior (Figure 5B). The dependence of the
247 two observed rates constants on drug concentration is linear for one of them (Figure 5C) and
248 non-linear for the other with an apparent plateau at approximately $16 \pm 2 \text{ s}^{-1}$ (Figure 5D). The
249 step with linear inhibitor concentration dependence corresponds to the second-order binding
250 step, whereas a non-linear concentration dependency hints at protein conformational
251 transitions. For a hyperbolic increase of the observed rate with substrate concentrations, one
252 cannot *a priori* differentiate between a conformational selection and an induced fit mechanism.
253 However, conformational selection happens before drug binding, and the intrinsic slow DFG-*in*
254 to DFG-*out* interconversion in Aurora A revealed by Gleevec binding (Figure 3A) must,
255 therefore, be unaltered. Since the apparent rate of $16 \pm 2 \text{ s}^{-1}$ (Figure 5D) is two orders of
256 magnitude faster, it can only reflect an induced-fit step (i.e., $k_{obs} = k_3 + k_{-3}$).

257 So, what happened to the conformational selection step? We hypothesize that the lack
258 of this step in our kinetic traces is due to a too small amplitude of this phase, or not observable
259 because of photobleaching having a bigger effect at the longer measurement times. To lessen
260 potential photobleaching, we reduced the enzyme concentration and increased the temperature
261 to 35 °C. Indeed, under these conditions, the slow DFG-*in* to DFG-*out* kinetics were observed
262 as an increase of fluorescence intensity over time with an observed rate constant of
263 approximately 0.1 s^{-1} (Figure 5-figure supplement 1A).

264 While these experiments clearly establish the three-step binding mechanism, it does not
265 provide accurate rate constants for the conformational selection step and it cannot be observed
266 at 25 °C where all the other kinetic experiments are performed. To resolve this issue, we
267 repeated the Aurora A–Gleevec experiment at 25 °C (Figure 5-figure supplement 2A, B) and
268 obtained reliable rate constants ($k_1 = 0.09 \pm 0.01 \text{ s}^{-1}$ and $k_{-1} = 0.06 \pm 0.005 \text{ s}^{-1}$) for the
269 conformational selection step in Aurora A, which will be used as “knowns” in what follows. We
270 hypothesize that the conformational selection step reflects the interconversion between
271 inactive/active conformations and is correlated with the DFG-*out* and -*in* position (Figure 1). The
272 following observations support our hypothesis: (i) two crystal structures for the apo-protein show

273 Trp277 in very different environments (Figure 1E), (ii) Danusertib has been proposed to
274 selectively bind to the DFG-out conformation based on a co-crystal structure (Figure 5A)
275 (Fancelli et al., 2006), and (iii) the same slow step is observed for binding of both Gleevec and
276 Danusertib.

277 Next, the dissociation kinetics for Danusertib was measured by fluorescence and
278 appeared to be extremely slow with an observed slow-off rate of $(3.2 \pm 0.3) \times 10^{-4} \text{ s}^{-1}$ (Figure
279 5E). Rationalization of complex binding kinetics cannot be done anymore by visual inspection
280 and kinetic intuition, which can, in fact, be misleading. In order to elucidate the correct binding
281 mechanism and obtain accurate kinetic parameters, all kinetic traces were globally fit (Figure 6)
282 to the three-step binding scheme (Figure 5I). Although global fitting of the binding and
283 dissociation kinetics in KinTek Explorer delivered a value for k_{-2} , evaluation of the kinetic
284 scheme with respect to the time traces exposes that k_{-2} is not well determined from our
285 experiments. We therefore designed a double-jump experiment to populate the $\text{AurA}_{\text{out}}\cdot\text{D}$ state
286 followed by dissociation to obtain more accurate information on k_{-2} . Our stopped-flow machine
287 lacks the capability to perform double mixing. Therefore, the double-jump experiment was
288 performed using a Creoptix WAVE instrument. This label-free methodology uses waveguide
289 interferometry to detect refractive index changes due to alteration in surface mass in a vein
290 similar to Surface Plasmon Resonance (SPR). It is an orthogonal technique that sidesteps
291 notable issues associated with fluorescence methods (e.g., photobleaching and inner-filter
292 effects). In short, after immobilizing Aurora A on a WAVEchip, a high concentration of
293 Danusertib was injected for a short, variable period of time, and dissociation was triggered by
294 flowing buffer through the microfluidics channel to remove the drug. The dissociation kinetics fit
295 to a single exponent with a rate constant, k_2 , of $6.8 \pm 0.4 \text{ s}^{-1}$ (Figure 5F and Figure 5-figure
296 *supplement 1B*).

297 We want to discuss a few additional kinetic features. First, the observed rate constant
298 measured in the dilution experiment (Figure 5E, $k_{-3} = (3.2 \pm 0.3) \times 10^{-4} \text{ s}^{-1}$) is slower than k_{-3}
299 from the global fit ($k_{-3} = (7.1 \pm 0.5) \times 10^{-4} \text{ s}^{-1}$), which might seem counterintuitive. The observed
300 rate constant was verified by an additional dilution experiment using Creoptix WAVE ($k_{-3} = (2 \pm$
301 $0.6) \times 10^{-4} \text{ s}^{-1}$, Figure 5-figure supplement 1C). The difference in the observed and microscopic
302 rate constant can, however, be fully reconciled by considering the kinetic partitioning for the
303 proposed scheme, as shown in Figure 6-figure supplement 1. Second, a powerful and
304 independent validation of the three-step binding mechanism is obtained by comparing the
305 measured overall K_D of Danusertib with the calculated macroscopic K_D from the microscopic
306 rate constants (Figure 5G, H, I and Figure 5-figure supplement 1D) according to Equation 4,

307 which indeed delivers values that are within experimental error. In addition, our values for k_2 ,
308 k_{-3} , and K_D are in good agreement with those reported in a recent study using SPR (Willemsen-
309 Seegers et al., 2017).

310 Our results illuminate trivial but profound principles of binding affinity and lifetime of
311 drug/target complexes: a conformational selection mechanism always weakens the overall
312 inhibitor affinity, while an induced-fit step tightens the affinity depending on how far-shifted the
313 equilibrium in the enzyme/drug complex is (Equations 2-4, Figure 6-figure supplement 2). For
314 DFG-*out* binders (e.g., Danusertib and Gleevec), the DFG-*in* and -*out* equilibrium weakens the
315 overall affinity 1.6-fold; however, the conformational change after drug binding results in a four
316 orders of magnitude tighter binding for Danusertib and is the sole reason for its high affinity to
317 Aurora A compared to Gleevec. The dissociation constants for the bimolecular binding step K_2
318 is very similar for both inhibitors. Finally, the lifetime of Danusertib on the target is very long
319 because of the very slow conformational dynamics within the Aurora A/Danusertib complex (k_{-3}
320 = $(7.1 \pm 0.5) \times 10^{-4} \text{ s}^{-1}$). Earlier examples of protein kinases that also show remarkable slow off-
321 rates, presumably caused by conformational changes, include the epidermal growth factor
322 receptors (Berezov, Zhang, Greene, & Murali, 2001; Wood et al., 2004) and CDK8 (Schneider,
323 Bottcher, Huber, Maskos, & Neumann, 2013) amongst others (Willemsen-Seegers et al., 2017).
324 To the best of our knowledge, we present here for the first time a detailed stopped-flow kinetics
325 analysis for Aurora A that unequivocally shows the slow off-rate is caused by the conformational
326 change within the drug-bound state, and not the dissociation step.

327

328 **Kinetics of AT9283 binding to Aurora A – a surprise**

329 We chose AT9283 as a third inhibitor to characterize the binding mechanism because it has
330 been described as a DFG-*in* binder based on a crystal structure of AT9283 bound to Aurora A
331 (PDB 2W1G, (Howard et al., 2009)). We, therefore, anticipated that in its binding kinetics one
332 can now detect the DFG-*out* to DFG-*in* switch. Rapid kinetic experiments of binding AT9283 to
333 Aurora A at 25 °C resulted in biphasic traces and both processes showed an increase in
334 fluorescence over time (Figure 7A). The k_{obs} for the faster phase (k_2) was linearly dependent on
335 drug concentration reflecting the binding step (Figure 7B) and k_{obs} for the slower phase (k_3) has
336 a limiting value of $0.8 \pm 0.2 \text{ s}^{-1}$ and is attributed to an induced-fit step (Figure 7C). For the
337 conformational selection step (i.e., DFG-*out* to DFG-*in*), a decrease in fluorescence is expected
338 because for the reverse flip observed in the Gleevec and Danusertib experiments, a
339 fluorescence increase was seen (Figure 3A and Figure 5-figure supplement 1A). However, we

340 could not find any condition (e.g., by varying temperature and ligand concentrations) where
341 such a phase could be observed.

342 Dissociation is characterized by double-exponential kinetics (Figure 7D and Figure 7-
343 *figure supplement 1A*). The fast phase (~38% of the total amplitude change) decays with a rate
344 constant of $(1.1 \pm 0.02) \times 10^{-2} \text{ s}^{-1}$, and the slow phase (~62% of the total change in amplitude)
345 has a rate constant of $(0.1 \pm 0.01) \times 10^{-2} \text{ s}^{-1}$. To distinguish between the reverse induced-fit step
346 (k_{-3}) and the physical dissociation step (k_{-2}), a double-jump experiment was performed that
347 unambiguously assigned the faster phase to k_{-2} (Figure 7E and Figure 7-*figure supplement*
348 *1B*). Our attempts to globally fit all kinetic traces assuming binding to only the DFG-*in* state and
349 using the rate constants for the DFG-loop flip from the Gleevec experiment failed (Figure 8-
350 *figure supplement 1A*). An extended model, where AT9283 can bind to both DFG_{in/out}
351 conformations, followed by a common induced-fit step can also not explain the experimental
352 kinetic traces (Figure 8-*figure supplement 1B*). These failures, together with the lack of a
353 detectable conformational selection step, led to a new model in which both the DFG-*in* and
354 DFG-*out* states can bind AT9283, but only AurA_{in}:AT can undergo an induced-fit step (Figure
355 7H). All data can be globally fit to this model (Figure 8) and the overall K_D calculated from the
356 corresponding microscopic rate constants (using Equation 5) is in good agreement with the
357 experimentally measured K_D (Figure 7F-H). Finally, the 10-fold difference between the k_{-3} from
358 the global fit (Figure 7H) and the experimentally observed slow off-rate can be reconciled by
359 kinetic partitioning as shown in Figure 7-*figure supplement 1A*.

360

361 **Crystal structures of AT9283 bound to Aurora A buttress new binding model**

362 In an effort to structurally verify our model we solved a crystal structure of Aurora A with AT9283
363 bound and indeed observed the DFG-*out* conformation (PDB 6CPG, Figure 9B and Table 1), in
364 contrast to the DFG-*in* conformation as previously reported (Figure 9A) (Howard et al., 2009).
365 Our structure was obtained by co-crystalizing Aurora A with AT9283 and a monobody that binds
366 to the same site as the natural allosteric activator TPX2 (Figure 9B). Binding of this monobody
367 shifts Aurora A into an inactive conformation, with the DFG-loop in the *out* conformation. This
368 new structure underscores the plasticity of Aurora A kinase and the ability of AT9283 to bind to
369 a DFG-*out* state, in addition to the previously reported DFG-*in* state.

370 Thus, our structural and kinetic data together support that AT9283 can bind to both
371 DFG-*in* and DFG-*out* state of Aurora A, and emphasizes the need for caution when interpreting
372 single X-ray structures.

373

374 **Inhibitors take advantage of built-in dynamics for ATP binding**

375 We finally compared the binding kinetics of the ATP-competitive inhibitors described above with
376 the natural kinase substrate, ATP (Figure 10). In order to measure stopped-flow kinetics for ATP
377 binding, FRET was measured by exciting Trp residues in Aurora A and detecting fluorescence
378 transfer to the ATP-analogue mant-ATP (Lemaire, Tessmer, Craig, Erie, & Cole, 2006; Ni,
379 Shaffer, & Adams, 2000). The binding of mant-ATP to Aurora A showed biphasic kinetic traces
380 (Figure 10A) that describe the physical binding step (i.e., linear dependence on mant-ATP
381 concentration; Figure 10B) and the induced-fit step (Figure 10C). The observed rate constant
382 approaches a maximum value defined by the sum of $k_3 + k_{-3}$ (Figure 10C) and the intercept
383 can be estimated to be k_{-3} and is consistent with the value obtained from the k_{off} experiment
384 (Figure 10D). We find that mant-ATP can bind to both the DFG-*in* or -*out* conformations,
385 consistent with our nucleotide-bound crystal structures (Figure 1A-D) and recent single-
386 molecule fluorescence spectroscopy data that indicates that nucleotide binding does not
387 significantly affect this equilibrium (Cyphers, Ruff, Behr, Chodera, & Levinson, 2017). To confirm
388 the model, the kinetic data were globally fit to a two-step binding mechanism (Figure 10H, G).
389 The calculated K_D from the corresponding microscopic rate constants (Figure 10H) is
390 comparable with experimental macroscopic K_D obtained from a titration experiment (Figure 10E,
391 F).

392 The presence of an induced-fit step for the natural substrate ATP suggests that such
393 conformational change after ligand binding is a built-in property of the enzyme. In other words,
394 inhibitors take advantage of the inherent plasticity of the enzyme that is required for its activity
395 and regulation. The main difference between ATP and inhibitor binding is the rate constant for
396 the reverse induced-fit step (k_{-3}). In the case of ATP, this rate is much faster and, therefore,
397 does not significantly increase the overall affinity. Faster conformational changes and weaker
398 binding are of course prerequisites for efficient turnover; whereas slow conformational changes,
399 particularly the reverse induced-fit step, are at the heart of action for an efficient drug, because it
400 results in tight binding and a long lifetime on the target. In summary, binding of different ligands
401 to the ATP-binding site, such as nucleotides or ATP-competitive inhibitors, is comprised of the
402 physical binding step followed by an induced-fit step. By definition, it is the nature of the
403 induced-fit step that varies for the different ligands since it happens as a result of ligand binding.

404

405 **Discussion**

406 Characterizing the detailed kinetic mechanisms of drug binding is not just an academic exercise
407 but delivers fundamental knowledge for developing selective inhibitors with high affinity. An

408 induced-fit step turns out to be key for all tight-binding inhibitors studied. From our results on
409 Aurora A kinase presented here and earlier data on Tyrosine-kinases (Agafonov et al., 2014;
410 Wilson et al., 2015), we propose that this may be a general mechanism for different kinases and
411 multiple inhibitors, thereby providing a platform for future computational and experimental efforts
412 in rational drug design. Albeit, we note that verification of this proposition requires a larger
413 sampling of small molecules and different protein kinases throughout the kinome.

414 The “use” of a highly-skewed equilibrium towards E*:D for a promising drug is logical for
415 the following reasons: (i) it increases the affinity for the drug by this coupled equilibrium, (ii) it
416 prolongs the residence time of the drug on the target due to the often slow reverse rate, (iii) it is
417 specific for each drug as it happens after the drug binding, and (iv) it can add selectivity for the
418 targets because it likely involves residues more remote from the active site. An increased drug
419 residence time has significant pharmacological advantages as it can lead to a prolonged
420 biological effect, a decrease of side effects, and a lower risk of metabolic drug modification.
421 Such inhibitors have long been described as slow tight-binding inhibitors (Copeland, 2016;
422 Copeland, Pompliano, & Meek, 2006). The concept of the advantageous roles of induced-fit
423 steps is based on simple thermodynamics and protein flexibility, and is, therefore, likely of
424 relevance for drug design to other targets outside of the kinome.

425 Additionally, our data provides unique insight into the extensively discussed DFG flip.
426 Combining x-ray crystallography, NMR spectroscopy and stopped-flow kinetics of drug binding
427 establish the nature of this DFG flip both structurally, thermodynamically and kinetically, and
428 resolves the longstanding question of its role for drug affinity and selectivity. Selective binding of
429 a specific DFG-state by Gleevec has been first proposed as the reason for selectivity towards
430 Abl. This conformational selection principle has ever since been at the center of drug discovery
431 for many kinases, including Aurora A (Badrinarayan & Sastry, 2014; Liu & Gray, 2006). Based
432 on our results, we argue that conformational selection of the DFG-state by ATP-competitive
433 inhibitors is a mistakenly pursued concept in drug design for the following reasons: (i)
434 conformational selection by definition weakens the overall ligand affinity, (ii) active site binders
435 are automatically inhibitors, therefore selective binding to a specific DFG-state has no
436 advantage (Badrinarayan & Sastry, 2014; Liu & Gray, 2006), (iii) kinases interconvert between
437 both states. High selectivity gained by DFG-state selective binding could only be achieved in the
438 scenario of a highly skewed population towards the binding-competent state for one kinase
439 relative to all others, which is unfounded.

440 Our results exemplify why rational drug design is so challenging. The characterization of
441 the complete free-energy landscape of drug binding is needed, which will require more

442 sophisticated computational approaches guided by experimental data such as provided in our
443 study. A good illustration of this point are the computational reports that focused on the DFG flip
444 as a key determinant drug selectivity (Badrinarayan & Sastry, 2014) that now have been ruled
445 out by our kinetic measurements. Our data suggest that future design efforts should be focusing
446 on understanding and exploiting induced-fit steps. To this end, the different dynamic
447 personalities of kinases or, more general, drug targets need to be investigated at atomic
448 resolution and used to guide small-molecule design. The findings presented here are
449 encouraging for developing selective inhibitors even for kinases with very similar folds and drug
450 binding pockets since the action does not happen on a single structural element of the protein,
451 but on a complex energy landscape that is unique to each kinase.

452

453

454 **Materials and Methods**

455

456 **Cloning, expression and purification of dephosphorylated Aurora A (122-403) and** 457 **inhibiting monobody.**

458 Dephosphorylated Aurora A proteins were expressed and purified as described before (Zorba et
459 al., 2014) and analyzed by mass spectrometry to confirm their phosphorylation state. The
460 W227L mutant was generated using the QuickChange Lightning site-directed mutagenesis kit
461 (Agilent).

462 U-[¹⁵N] Aurora A was obtained by growing *E. coli* BL21(DE3) (New England Biolabs) in
463 M9 minimal medium containing 1 g/L ¹⁵NH₄Cl (Cambridge Isotope Laboratories, Tewksbury,
464 MA, USA) and 5 g/L D-glucose as the sole nitrogen and carbon source, respectively. [¹⁵N]-Trp
465 labeled wild-type Aurora A was obtained using the standard M9 minimal medium,
466 complemented with all amino acids (0.5 g/L) with the exception of tryptophan. One hour prior to
467 induction, 30 mg/L of ¹⁵N₂-L-Trp (NLM-800; Cambridge Isotope Laboratories, Tewksbury, MA,
468 USA) was added to the medium. Similarly, to obtain samples of wild-type and W277L Aurora A
469 containing 5-fluoro-tryptophan, bacterial growth was performed in unlabeled M9 medium
470 containing all amino acids (0.5 g/L) except for tryptophan. One hour before protein induction, the
471 media was supplemented with 30 mg/L of 5-fluoro-DL-tryptophan (Sigma-Aldrich) (Crowley,
472 Kyne, & Monteith, 2012). NMR samples contained 200-300 μM Aurora A in 50 mM HEPES, pH
473 7.3, 50 mM NaCl, 20 mM MgCl₂, 5 mM TCEP, 2 M TMAO and 10%(v/v) D₂O.

474 Inhibiting monobody used for co-crystallization with Aurora A and AT9283 was
475 expressed in *E. coli* BL21(DE3) cells harboring the plasmid pHBT containing His₆-tagged-Mb. A

476 culture of TB media containing 50 $\mu\text{g}/\text{mL}$ kanamycin that was grown overnight at 37 $^{\circ}\text{C}$ was
477 added to 1L of TB media with 50 $\mu\text{g}/\text{mL}$ kanamycin to get a starting OD_{600} of ~ 0.2 . This culture
478 was grown at 37 $^{\circ}\text{C}$ until the OD_{600} reached ~ 0.8 . Protein expression was induced by 0.6 mM
479 IPTG at 18 $^{\circ}\text{C}$ for 13-15 h and cells were harvested by centrifugation. The cell pellet was
480 resuspended in binding buffer (50 mM Tris-HCl, pH 8.0, 300 mM NaCl, 20 mM imidazole, 20
481 mM MgCl_2 , 10% glycerol) containing 0.5 mg/mL lysozyme, 5 $\mu\text{g}/\text{mL}$ DNase, and 1x EDTA-free
482 protease inhibitor cocktail. Cells were ruptured by sonication on ice then centrifuged at 18,000
483 rpm at 4 $^{\circ}\text{C}$ for 1 h. The supernatant was loaded onto HisTrapTM HP (GE Healthcare) after
484 filtration using 0.22 μm filtering unit. The pellet was resuspended with GuHCl buffer (20 mM
485 Tris-HCl, pH 8.0, 6 M GuHCl) and allowed to rotate on wheel for 10 min at 4 $^{\circ}\text{C}$ and spun down
486 again. The supernatant was passed through 0.2 μm filtering unit and loaded onto HisTrapTM HP
487 column previously loaded with soluble fraction and pre-equilibrated with GuHCl buffer. Refolding
488 monobody on-column was achieved by washing the HisTrapTM HP column with 5 column
489 volumes (CV) of GuHCl buffer, followed by 5 CV of Triton-X buffer (binding buffer + 0.1% Triton
490 X-100), then 5 CV of β -cyclodextrin buffer (binding buffer + 5 mM β -cyclodextrin), and finally 5
491 CV of binding buffer. Monobody was eluted with 100% of elution buffer (binding buffer + 500
492 mM imidazole). The protein was dialyzed overnight in gel-filtration buffer (20 mM Tris-HCl, pH
493 7.5, 200 mM NaCl, 20 mM MgCl_2 , 5 mM TCEP, 10% glycerol) in the presence of TEV protease
494 (1:40 TEV:P:Mb molar ratio). After dialysis, the TEV-cleaved monobody was passed through
495 HisTrapTM HP column again. The flow-through containing TEV-cleaved monobody was collected
496 and concentrated before loading onto Superdex 200 26/60 gel-filtration column pre-equilibrated
497 with the gel-filtration buffer. The monobody was flash-frozen and stored in -80 $^{\circ}\text{C}$ until use.

498

499 **X-ray crystallography**

500 Crystals of dephosphorylated (deP) Aurora A¹²²⁻⁴⁰³ + AMPPCP were obtained by mixing 570 μM
501 (18 mg/mL) deP Aurora A¹²²⁻⁴⁰³ and 1 mM AMPPCP in a 2:1 ratio with mother liquor (0.2 M
502 ammonium sulfate, 0.2 M Tris-HCl, pH 7.50, 30% (w/v) PEG-3350). The crystals were grown at
503 18 $^{\circ}\text{C}$ by vapor diffusion using the hanging-drop method. The protein used for the crystallization
504 was in storage buffer (20 mM Tris-HCl, pH 7.5, 200 mM NaCl, 10% (v/v) glycerol, 20 mM MgCl_2 ,
505 1 mM TCEP); AMPPCP was freshly prepared before use in the same buffer. Crystals were
506 flash-frozen in liquid nitrogen prior to shipping. Crystals of apo, deP Aurora A¹²²⁻⁴⁰³ were grown
507 at 18 $^{\circ}\text{C}$ by vapor diffusion using the sitting-drop method (96-well plate). A 1:1 ratio of protein to
508 mother liquor was obtained by combining 0.5 μL of 300 μM (10 mg/mL) deP Aurora A¹²²⁻⁴⁰³ in

509 50 mM HEPES, pH 7.3, 500 mM ammonium acetate, 1 mM MgCl₂, 5 mM TCEP) with 0.5 μL of
510 0.15 M Tris-HCl, pH 7.5, 0.15 M ammonium sulfate, 35% (w/v) PEG-3350. Crystals were
511 soaked for 10-20 s in cryo buffer (20% (w/v) PEG-400, 20% ethylene glycol, 10% water and
512 50% mother liquor) before flash-freezing in liquid nitrogen. The complex between Aurora
513 A¹²²⁻⁴⁰³, inhibiting monobody (Mb) and AT9283 was crystallized at 18 °C by vapor diffusion
514 using the sitting-drop method. In short, a 1:1 ratio of protein mixture to mother liquor was
515 obtained by combining 0.5 μL of sample [240 μM deP Aurora A¹²²⁻⁴⁰³ + 1.0 mM AT9283
516 + 250 μM Mb] with 0.5 μL of mother liquor [0.1 M Bis-Tris, pH 5.5, 0.2 M magnesium chloride,
517 19% (w/v) PEG-3350]. Crystals were soaked for 10-20 s in cryo buffer (17.5% (w/v) PEG-400,
518 17.5% ethylene glycol, 45% water and 20% mother liquor) before flash-freezing in liquid
519 nitrogen.

520 Diffraction data were collected at 100 K at the Advanced Light Source (Lawrence
521 Berkeley National Laboratory) beamlines ALS 8.2.1 (apo-AurA and AurA+Mb+AT9283) and
522 8.2.2 (AurA+AMPPCP) with a collection wavelength of 1.00 Å.

523 Data were indexed and integrated using iMOSFLM (Battye, Kontogiannis, Johnson,
524 Powell, & Leslie, 2011) for apo/AMPPCP-bound Aurora A and Xia2 (Winter, 2010) using XDS
525 (Kabsch, 2010) for the Aurora A/Mb/AT9283 complex, respectively. Data were scaled and
526 merged with AIMLESS (Evans & Murshudov, 2013), in the case of Aurora A/Mb/AT9283 two
527 data separate data sets were merged. All software was used within the CCP4 software suite
528 (Winn et al., 2011).

529 As initial search models 1MQ4 (Nowakowski et al., 2002) and 3K2M (Wojcik et al., 2010)
530 were used for Aurora A and monobody, respectively, and molecular replacement was performed
531 using Phaser (McCoy et al., 2007). The molecules were placed in the unit cell using the
532 ACHESYM webserver (Kowiel, Jaskolski, & Dauter, 2014). Iterative refinements were carried
533 out with PHENIX (Adams et al., 2010), using rosetta.refine (DiMaio et al., 2013) and
534 phenix.refine (Afonine et al., 2012), and manual rebuilding was performed in Coot (Emsley &
535 Cowtan, 2004; Emsley, Lohkamp, Scott, & Cowtan, 2010).

536 Structure validation was performed using MolProbity (V. B. Chen et al., 2010) and
537 yielded the statistics given below. The Ramachandran statistics for dephosphorylated apo
538 (AMPPCP-bound) Aurora A are: favored: 93.65 (94.90)%, allowed 5.95 (4.71)%, outliers: 0.4
539 (0.39)%; 0.48 (0.0)% rotamer outliers and an all-atom clashscore of 4.45 (2.44). For the
540 Aurora A/Mb/AT9283 complex, the Ramachandran statistics are: favored: 92.64%, allowed
541 7.06%, outliers: 0.3%); 0.0 % rotamer outliers and an all-atom clashscore of 2.81. We note that
542 the B-factors for the monobodies in the complex of Aurora A/Mb/AT9283 are rather high,

543 indicating significantly flexibility in the parts that are not part of the binding interface with Aurora
544 A.

545 The data collection and refinement statistics are given in Table 1. Structure factors and
546 refined models have been deposited in the PDB under accession codes: 6CPE (apo Aurora A),
547 6CPF (Aurora A + AMPPCP) and 6CPG (Aurora A/Mb/AT9283).

548

549 All figures were generated using Chimera (Pettersen et al., 2004).

550

551 **NMR spectroscopy**

552 All ^{19}F NMR experiments were performed at 35 °C on a Varian Unity Inova 500 MHz
553 spectrometer, equipped with a $^1\text{H}/^{19}\text{F}$ switchable probe tuned to fluorine (90° pulse width of 12
554 μs). All 1D ^{19}F spectra were recorded with a spectral width of ~60 ppm and a maximum
555 evolution time of 0.25 s. An interscan delay of 1.5 s was used with 5,000 scans per transients,
556 giving rise to a total acquisition time of 2.5 h per spectrum. To remove background signal from
557 the probe and avoid baseline distortions, data acquisition was started after a ~100 μs delay
558 (using the "delacq" macro) and appropriate shifting of the data followed by backward linear
559 prediction was performed. The data were apodized with an exponential filter (2.5 Hz line
560 broadening) and zero-filled before Fourier transform. To improve the signal-to-noise ratio
561 several data sets were recorded consecutively and, provided that the sample remained stable,
562 added together after processing (two for apo Aurora A, four for Aurora A + AMPPCP, and five
563 for W277L + AMPPCP, respectively). ^{19}F chemical shifts were referenced externally to
564 trifluoroacetic acid (TFA) at -76.55 ppm.

565 $[^1\text{H}-^{15}\text{N}]$ -TROSY-HSQC experiments were recorded at 25 °C on an Agilent DD2 600
566 MHz four-channel spectrometer equipped with a triple-resonance cryogenically cooled probe-
567 head. Typically, 115–128 (^{15}N) \times 512 (^1H) complex points, with maximum evolution times equal
568 to 48.5–64 (^{15}N) \times 64 (^1H) ms. An interscan delay of 1.0 s was used along with 32 or 56 scans
569 per transient, giving rise to a net acquisition time 1.5-2.5 h for each experiment. To improve the
570 signal-to-noise ratio several data sets were recorded consecutively and, provided that the
571 sample remained stable, added together after processing (typically three data sets per sample).

572 All data sets were processed with the NMRPipe/NMRDraw software package (Delaglio
573 et al., 1995) and 2D spectra were visualized using Sparky (Goddard, 2008). Deconvolution of
574 the ^{19}F spectra and line shape fitting was performed using the Python package nmrglue
575 (Helmus & Jaroniec, 2013).

576

577 **Kinetics experiments of Aurora A with Gleevec, Danusertib, and AT9283**

578 **Stopped-flow experiment.** Intrinsic tryptophan fluorescence spectroscopy was used to monitor
579 drug binding kinetics to Aurora A. All experiments were performed at 25 °C, except for the
580 Gleevec kinetics that were measured at 10 °C (unless otherwise stated) because the binding of
581 Gleevec to Aurora A is too fast, $k_{obs, Binding}$. Stock solutions of 200 mM Danusertib, 200 mM
582 AT9283 and 50 mM Gleevec (all purchased from Selleck Chemicals,
583 <http://www.selleckchem.com>) were prepared in 100% DMSO were and stored at -80 °C until
584 used. Aurora A used in the kinetic experiments was dephosphorylated Aurora A as determined
585 by mass spectrometry, Western blot and activity experiments (data not shown). The rapid
586 kinetics were studied using a stopped-flow spectrophotometer (SX20 series from Applied
587 Photophysics Ltd). The flow system was made anaerobic by rinsing with degassed buffer
588 comprised of 50 mM HEPES, 50 mM NaCl, 20 mM MgCl₂, 5 mM TCEP, 5% DMSO, pH 7.30 to
589 minimize photobleaching. The stock solutions of Aurora A and all drugs were made anaerobic
590 by degassing with ThermoVac (MicroCal) at the desired temperature. In general, a solution of 5
591 μM Aurora A was loaded in one syringe and quickly mixed with drug, prepared in the same
592 buffer, in the other syringe (mixing ratio 1:10). A significant increase or decrease in the
593 fluorescence intensity of Aurora A (excitation at 295 nm, emission cut-off at 320 nm) can be
594 observed due to the drug binding. For each drug concentration, at least five replicate
595 measurements were made and these transients were averaged. Analysis was performed by
596 fitting the individual trace to exponential equations using Pro-Data Viewer (Applied
597 Photophysics Ltd) or with Kinesyst 3 software (TgK Scientific) and error bars denote the
598 standard errors as obtained from the fit. KaleidaGraph version 4.5.3 (Synergy) was used for
599 data analysis and plotting. All kinetic data were globally fitted in KinTek Explorer software
600 (Johnson, 2009; Johnson, Simpson, & Blom, 2009).

601 Under the rapid equilibrium approximation, the binding and dissociation steps of Gleevec
602 to Aurora A are fast compared to conformational selection, therefore the value of k_1 and k_{-1} can
603 be estimated according to Equation 1:

604

605
$$k_{obs} = \frac{k_{-1}}{1 + \left(\frac{[Gleevec]}{[Aurora A] + \left(\frac{k_{-2}}{k_2} \right)} \right)} + k_1$$
 Equation 1

606

607 where k_1 and k_{-1} represent the conformational change from DFG-*in* to -*out* and vice versa,
608 respectively. The approximate values of k_1 and k_{-1} obtained from fitting to this equation are
609 used as starting values for the global fit.

610 For the 5 μ M Aurora A/Gleevec complex, the release of the drug was recorded after a
611 11-fold dilution of the complex using the stopped-flow instrument for 0.25 s (excitation at 295
612 nm, emission cut-off at 320 nm) at 10 °C.

613

614 **Creoptix WAVE experiments.** Double jump, slow-off, and macroscopic K_D experiments of
615 Aurora A with drugs were studied using a Creoptix WAVE instrument (Creoptix AG, Wädenswil,
616 Switzerland) at 25 °C. All chemicals were purchased from GE Healthcare, unless otherwise
617 stated. The protocols in the WAVEcontrol software for conditioning of the chip, immobilization of
618 proteins and performing kinetics experiments were followed. In short, the polycarboxylate chip
619 (PCH) was activated by injection of a 1:1 mixture with final concentrations of 200 mM N-ethyl-
620 N'-(3-dimethylaminopropyl)carbodiimide (EDC) and 50 mM N-hydroxysuccinimide (NHS),
621 followed by streptavidin immobilization (50 μ g/mL in 10 mM sodium acetate pH 5.0). Unreacted
622 sites on the chip were blocked with 1 M ethanolamine pH 8.0. For all activation, immobilization
623 and passivation steps 0.2x HBS-EP was used as running buffer with a flowrate of 10 μ L/min and
624 an injection duration of 420 s on both channels 1 and 2.

625 Biotinylated T288V variant that mimics dephosphorylated Aurora A was used for
626 experiments performed on the Creoptix WAVE instrument. The activity of T288V with substrate
627 Lats2, the macroscopic K_D and slow-off rate of Danusertib were the same as wild-type (data not
628 shown). Biotinylated T288V Aurora A (70 μ g/mL) was immobilized on the PCH-streptavidin chip
629 with 10 μ L/min injection and 15 s injection duration over channel 1 only (channel 2 was used as
630 reference channel). All experiments were run in 50 mM HEPES, 50 mM NaCl, 20 mM MgCl₂, 5
631 mM TCEP, 0.03 mg/mL BSA, 0.005% Tween-20, pH 7.30 as running buffer. Binding
632 experiments were evaluated over a range of Danusertib (0.13 – 66.67 nM), AT9283 (0.03 – 64.8
633 nM), and Gleevec (0.37 – 40 μ M) concentrations. Gleevec binding experiments contained 5%
634 DMSO in the running buffer (see above) to enhance Gleevec's solubility. Double-jump
635 experiments of Aurora A/drugs were performed by injecting 1 μ M Danusertib or AT9283 with
636 0.2, 0.4, 0.8, and 2 s injection duration for Danusertib and 1 and 3 s injection duration for
637 AT9283 followed by a 60 s dissociation duration per injection. The slow-off experiments were
638 performed by injecting 5 μ M Danusertib or AT9283 with 5-10 s injection duration (to fully

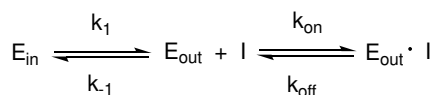
639 saturate Aurora A) followed by a 180 s injection of buffer to remove the excess drug and the
640 dissociation was measured for a duration of 10800 s.

641
642 **Spectrofluorometer experiments.** The spectrofluorometer FluoroMax-4 (Horiba Scientific) with
643 temperature controller was used to study the slow-off rate of Aurora A with Danusertib at 25 °C.
644 For this experiment, a solution containing 30 nM Aurora A and 30 nM Danusertib was pre-
645 incubated for an hour, before diluting 30-fold into degassed buffer (ratio 1:30). A significant
646 decrease in the fluorescence intensity of Aurora A (excitation at 295 nm, emission at 340 nm)
647 can be seen due to the Danusertib release. The fluorescence signal was recorded every 160 s
648 for a duration of six hours using the photobleaching minimization option that will close the
649 shutter after each acquisition. A control experiment was performed, using the same
650 experimental conditions, but without drug in order to account for photobleaching.

651
652 **Overall dissociation constant calculated from intrinsic rate constants.** In the following
653 equations, K_1 , K_2 , K_3 and K_4 equal to:

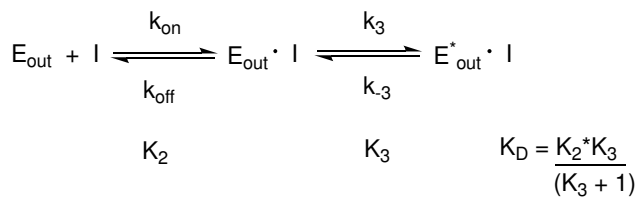
$$K_1 = \frac{k_{-1}}{k_1}$$
$$K_2 = \frac{k_{-2}}{k_2} = \frac{k_{off}}{k_{on}}$$
$$K_3 = \frac{k_{-3}}{k_3}$$
$$K_4 = \frac{k_{-4}}{k_4}$$

656
657 Conformational selection followed by inhibitor binding:



658 K_1 K_2 $K_D = (K_1 + 1) \cdot K_2$ Equation 2

659
660 Inhibitor binding followed by an induced-fit step:

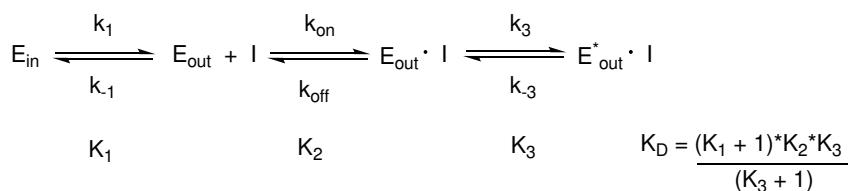


661

Equation 3

662

663 Conformational selection followed by inhibitor binding and an induced-fit step:



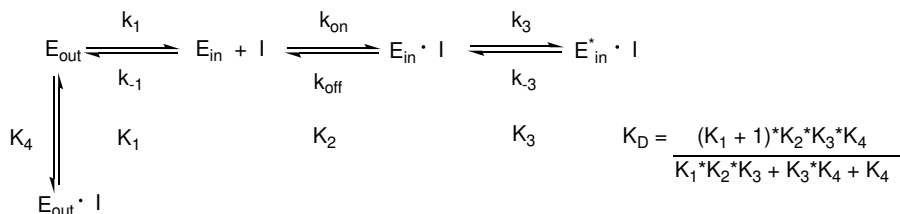
664

Equation 4

665

666 Conformational selection mechanism, followed by inhibitor binding to both DFG-*in* and -*out*
 667 state, but an induced-fit step only occurs in the DFG-*in* state:

668



669

Equation 5

670

671 The uncertainties in the calculated dissociation constant parameter using the equations above
 672 are obtained using standard error propagation.

673

674 **Aurora A binding to mant-ATP.** FRET using intrinsic tryptophan fluorescence is used to
 675 monitor mant-ATP (obtained from Jena Bioscience) binding kinetics to Aurora A at 10 °C. In the
 676 binding experiment or k_{on} , increasing concentration of mant-ATP were quickly mixed to 0.5 μM
 677 Aurora A (ratio 1:10, excitation at 295 nm, emission cut-off at 395 nm). In the experiment to
 678 measure the release of mant-ATP or k_{off} , 10 μM/10 μM Aurora A/mant-ATP complex was
 679 diluted with buffer (ratio 1:10). A significant decrease in the fluorescence intensity of Aurora A
 680 (excitation at 295 nm, emission cut-off at 395 nm) can be seen due to the mant-ATP release.

681

682 **Macroscopic dissociation constant experiments**

683 Fluorescence titration experiments were measured using FluoroMax-4 spectrofluorometer
 684 (Horiba Scientific). Increasing amounts of Aurora A/Danusertib complex (4 nM Aurora A and

685 150 nM Danusertib) or Aurora A/mant-ATP (1 μ M Aurora A and 2 mM mant-ATP) were titrated
686 into an Aurora A solution (4 nM and 1 μ M Aurora A for experiments with Danusertib and mant-
687 ATP, respectively). To measure Danusertib affinity, the excitation wavelength was 295 nm (5
688 nm bandwidth) and emission spectra were recorded from 310–450 nm (20 nm bandwidth) in
689 increments of 2 nm and the temperature was maintained at 25 °C. For the mant-ATP
690 experiment, the dissociation constant was measured at 10 °C using fluorescence energy
691 transfer from tryptophan residues in Aurora A to mant-ATP by setting the excitation wavelength
692 to 290 nm (5 nm bandwidth) and collecting the emission intensity from 310–550 nm (5 nm
693 bandwidth) in increments of 2 nm. A control experiment in the absence of Aurora A was
694 performed using the same experimental settings and used to correct for the mant-ATP
695 interference. In all experiments, a 5 minutes equilibration time was used after each addition of
696 Aurora A/Danusertib complex or Aurora A/mant-ATP complex.

697 The fluorescence intensity at 368 nm versus Danusertib concentration or the change in
698 fluorescence at 450 nm (ΔF^{450}) versus mant-ATP concentration was fitted to Equation 6 using
699 Levenberg-Marquardt nonlinear fitting algorithm included in KaleidaGraph to obtain the K_D .

700

$$701 \quad F = F_0 + A \cdot \frac{[I] + [E_t] + K_D - \sqrt{([I] + [E_t] + K_D)^2 - 4 \cdot [E_t] \cdot [I]}}{2 \cdot [E_t]} \quad \text{Equation 6}$$

702

703 F and F_0 are the fluorescence and initial fluorescence intensities, respectively. [I] and $[E_t]$ are
704 the total concentration of the drug or mant-ATP and the Aurora A, respectively.

705

706 **Acknowledgments**

707 We thank C. Sassetti (University of Massachusetts Medical School, Worcester) for the use of
708 the ESI-Q-TOF instrument, and the Advanced Light Source (ALS), Berkeley, CA, USA, for
709 access to beamlines BL8.2.1. and BL8.2.2. The Berkeley Center for Structural Biology is
710 supported in part by the National Institutes of Health, National Institute of General Medical
711 Sciences, and the HHMI. The ALS is supported by the Director, Office of Science, Office of
712 Basic Energy Sciences, of the U.S. Department of Energy under contract DE-AC02-
713 05CH11231. We thank Shohei and Akiko Koide (New York University) for the plasmid of the
714 monody used here. This work was supported by the Howard Hughes Medical Institute (HHMI);
715 the Office of Basic Energy Sciences, Catalysis Science Program, U.S. Dept. of Energy (award
716 DE-FG02-05ER15699); and the NIH (grant GM100966-01). R.O. was a HHMI Fellow of the
717 Damon Runyon Cancer Research Foundation (DRG-2114-12).

718

719 **Competing interests**

720 All authors declare no competing financial or other interests.

721

722 **Figures legends**

723

724 **Figure 1.** Dephosphorylated Aurora A samples both the active and inactive conformation. **(A)**
725 Superposition of X-ray structures of dephosphorylated Aurora A (residues 122-403) with
726 Mg^{2+} -AMPPCP (AMPPCP in gray sticks and magnesium as yellow sphere) in the inactive (cyan,
727 PDB 4C3R (Zorba et al., 2014)) and active (orange, PDB 6CPF) state, solved from crystals of
728 the same crystallization well. **(B)** Zoom-in of **(A)** to visualize the nucleotide binding region (K162,
729 D274, and E181), the R-spine (L196, Q185, F275, H254, and D311) and the activation loop
730 region (D256, K258, and T292). **(C)** Same zoom-in as in **(B)**, but dephosphorylated Aurora A in
731 active state (orange) is superimposed with phosphorylated Aurora A (red, PDB 1OL7 (Bayliss et
732 al., 2003)). **(D)** Superposition of the DFG(W) motif in the three states shown in **(B)** and **(C)**. **(E)**
733 Superposition of phosphorylated Aurora A in active conformation (red) and apo,
734 dephosphorylated Aurora A also in the active conformation (yellow, PDB 6CPE). **(F)** Zoom-in of
735 **(E)** showing the same region as in **(B)**.

736

737 **Figure 2.** NMR spectra indicate extensive dynamics of the DFG-loop. **(A)** The four tryptophan
738 residues in Aurora A are shown on the structure (PDB 4C3R (Zorba et al., 2014)) in stick
739 representation; Trp277 in the DFGW-loop is highlighted in red. **(B)** Overlay of $[^1H-^{15}N]$ -TROSY-
740 HSQC spectra of dephosphorylated Aurora A in its apo-state (U- $[^{15}N]$, blue; $[^{15}N]$ -Trp, green)
741 and AMPPCP-bound (U- $[^{15}N]$, red). Only three instead of the four expected cross peaks for
742 tryptophan side chains are detected. **(C)** ^{19}F NMR spectra of 5-fluoro-Trp labeled
743 dephosphorylated wild-type Aurora A (apo in blue and AMPPCP-bound in red) and the W277L
744 Aurora A mutant bound to AMPPCP (green). The assignment of Trp277 following the DFG-loop
745 is shown. **(D)** ^{19}F spectrum of wild-type Aurora A bound to AMPPCP (red) together with its
746 deconvolution into four Lorentzian line shapes, the overall fit is shown as a black, dotted line.
747 The integrals for all four signals are equal, but the linewidth for Trp277 (purple) is approximately
748 5-fold larger.

749

750 **Figure 3.** Kinetics of Gleevec binding to Aurora A at 10 °C measured by stopped-flow Trp
751 fluorescence to dissect all binding steps. **(A)** Kinetics after mixing 0.5 μ M Aurora A with 4.5 μ M

752 Gleevec is double exponential with a fast decrease and a slow increase in fluorescence signal.
753 (B) The decrease in fluorescence intensity due to the fast binding phase was completed within
754 0.25 s. (C) Observed rate constants of fast binding phase were plotted against increasing
755 concentrations of Gleevec ($k_{obs, Binding} = 1.1 \pm 0.3 \mu\text{M}^{-1}\text{s}^{-1}$, $k_{diss} = 31 \pm 2 \text{ s}^{-1}$ from the y-
756 intercept). (D) The increase in fluorescence intensity of slow phase (A) is attributed to
757 conformational selection. The plot of $k_{obs, CS}$ of this slow phase versus Gleevec concentration
758 was fit to Equation 1 and yields $k_1 = 0.014 \pm 0.001 \text{ s}^{-1}$ and $k_{-1} = 0.011 \pm 0.002 \text{ s}^{-1}$. (E)
759 Dissociation kinetics of pre-incubated solution with 5 μM Aurora A and 5 μM Gleevec measured
760 by stopped-flow fluorescence after an 11-fold dilution of the complex yields the $k_{-2} = 23.3 \pm 2 \text{ s}^{-1}$.
761 (F) The macroscopic dissociation constant (K_D) of Gleevec binding to Aurora A measured by
762 Creoptix WAVE. (G) Gleevec (labeled as G) binding scheme to Aurora A corresponds to a two-
763 step binding mechanism: conformational selection followed by the physical binding step. The
764 corresponding microscopic rate constants obtained from the global fit and calculated overall
765 equilibrium and dissociation constants are shown. Fluorescence traces are the average of at
766 least five replicate measurements ($n > 5$), and error bars and uncertainties given in C-G denote
767 the (propagated) standard deviation in the fitted parameter.

768
769 **Figure 4.** Global fits of Gleevec binding- and dissociation-kinetics to Aurora A at 10 °C. Fitting of
770 kinetic traces (average, $n > 5$) of the mixing of 0.5 μM Aurora A with different Gleevec
771 concentrations at two timescales, 0.25 s and 120 s, and dissociation kinetics (k_{off}) were
772 performed using the KinTek Explorer software with the binding scheme in Figure 3G. Red lines
773 show the results of the global fit to the experimental data in black.

774
775 **Figure 5.** Mechanism of Danusertib binding to Aurora A at 25 °C. (A) Danusertib bound to the
776 DFG-out conformation of Aurora A is shown highlighting important active-site residues in stick
777 representation (PDB 2J50 (Fancelli et al., 2006)). (B) The increase in fluorescence upon
778 Danusertib binding is fitted to a double exponential. (C) Plot of $k_{obs, Binding}$ versus the
779 concentration of Danusertib for the fast phase yields $k_2 = 0.4 \pm 0.1 \mu\text{M}^{-1}\text{s}^{-1}$ and $k_{-2} = 4.6 \pm 3 \text{ s}^{-1}$
780 and the $k_{obs, IF}$ for the slow phase (D) reaches a plateau around $16 \pm 2 \text{ s}^{-1}$. (E) Dissociation of
781 Danusertib from Aurora A at 25 °C after a 30-fold dilution of the Aurora A/Danusertib complex
782 measured by Trp-fluorescence quenching and fitting with single exponential gives a value of k_{-3}
783 $= (3.2 \pm 0.3) \times 10^{-4} \text{ s}^{-1}$. (F) Double-jump experiment (2 s incubation time of 1 μM Danusertib to
784 Aurora A followed by 60 s long dissociation step initiated by a wash with buffer) was measured

785 by Creoptix WAVE waveguide interferometry to properly define the value of $k_{-2} = 6.8 \pm 0.4 \text{ s}^{-1}$.
786 (G) Macroscopic dissociation constant (K_D) determined by Creoptix WAVE waveguide
787 interferometry: surface-immobilized Aurora A was incubated with various concentrations of
788 Danusertib (0.1 nM (black), 0.2 nM (blue), 0.4 nM (purple), 0.8 nM (red), 2.4 nM (green), 7.2 nM
789 (pink), 21.6 nM (cyan), and 64.8 nM (orange)) and surface mass accumulation was observed
790 until establishment of equilibrium. (H) A plot of the final equilibrium value versus Danusertib
791 concentration yields a $K_D = 1.1 \pm 0.4 \text{ nM}$. (I) Binding scheme of Danusertib (labeled D)
792 highlighting a three-step binding mechanism, containing both conformational selection and
793 induced-fit step. Red lines in (B, F) and black line in (E) are the results from fitting. Kinetic
794 constants shown in I determined from global fitting (Figure 6). Fluorescence traces are the
795 average of at least five replicate measurements ($n > 5$), and error bars and uncertainties given
796 in C-E, H, and I denote the (propagated) standard deviation in the fitted parameter.

797
798 **Figure 5-figure supplement 1.** (A) Kinetic trace at 35 °C of 18.2 μM Danusertib binding to 0.1
799 μM Aurora A. The red line represents the best fit of the trace to a double exponential function.
800 The initial fast increase in fluorescence is a convolution of the fast binding and induced-fit steps,
801 whereas the slower phase gives an observed rate constant of approximately 0.1 s^{-1} , suggestive
802 of a third process (i.e., conformational selection). (B) Double-jump experiments measured with
803 Creoptix WAVE waveguide interferometry at 25 °C using Danusertib and a 0.2, 0.4, 0.8 and 2
804 s incubation time. In the first step of the double jump, Danusertib is incubated with surface-
805 immobilized Aurora A kinase before washing with buffer alone initiates dissociation in a second
806 step. All traces show a single exponential decay with an observed rate constant of 6 s^{-1} and its
807 amplitude increases with longer incubation time as more $\text{AurA}_{\text{out}}:\text{D}$ is formed. (C) Dilution of the
808 Aurora A/Danusertib complex formed after 1 hour of incubation. The slow dissociation of Aurora
809 A/Danusertib (limited by k_3) was measured by Creoptix WAVE waveguide interferometry and
810 fitted to a single exponential with a value of $k_{-3} = (2 \pm 0.6) \times 10^{-4} \text{ s}^{-1}$. (D) Representative
811 selection of emission spectra obtained after the addition of increasing concentrations of
812 Danusertib (0-11.25 nM from dark to light blue) to Aurora A (excitation at 295 nm). Plot of the
813 increase in fluorescence intensity at 368 nm versus Danusertib concentration yields a K_D value
814 of $0.4 \pm 0.1 \text{ nM}$ determined by fitting the data to Equation 6. Fluorescence trace in A is the
815 average of five replicate measurements ($n = 5$), and the uncertainties given in D denotes the
816 standard deviation in the fitted parameter.

817

818 **Figure 5-figure supplement 2.** Kinetics of Gleevec binding to Aurora A at 25 °C to determine
819 DFG-*in*/DFG-*out* equilibrium in apo Aurora A at 25 °C. **(A)** 0.5 μM Aurora A was mixed with
820 indicated Gleevec concentrations. The increase in fluorescence intensity of slow phase reflects
821 the conformational selection step (see Figure 3A). **(B)** $k_{obs,CS}$ of the slow phase as a function of
822 the Gleevec concentration is an inverse hyperbolic function and fitting to Equation 1 gives $k_1 =$
823 $0.09 \pm 0.01 \text{ s}^{-1}$ and $k_{-1} = 0.06 \pm 0.005 \text{ s}^{-1}$. Corresponding binding scheme is depicted.
824 Fluorescence traces are the average of at least five replicate measurements ($n > 5$), and error
825 bars and uncertainties given in B denote the standard deviation in the fitted parameter.

826
827 **Figure 6.** Global fits of Danusertib binding and dissociation kinetics to Aurora A at 25 °C.
828 Binding kinetics was monitored by stopped-flow fluorescence for different concentrations of
829 Danusertib (indicated) to 0.5 μM Aurora A, and dissociation kinetics (k_{off}^{obs}) by Creoptix and
830 fluorimeter (see Figure 5). Fluorescence traces are the average of at least five replicate
831 measurements ($n > 5$). Global fitting was performed using the KinTek Explorer software using
832 the model shown in Figure 5I.

833
834 **Figure 6-figure supplement 1.** Kinetic partitioning of Aurora A with Danusertib. The apparent
835 discrepancy between the experimentally observed off rates and the microscopic rate constant,
836 k_{-3} , can be explained by considering the kinetic partitioning. Uncertainties given denote the
837 (propagated) standard deviation in the fitted parameter.

838
839 **Figure 6-figure supplement 2.** Effect of the equilibrium constant for the conformational
840 selection and induced-fit step on the overall K_D for Danusertib. The equilibrium constant was
841 changed in both directions by two orders of magnitude starting from unity for the conformational
842 selection (CS) mechanism **(A)** and induced-fit (IF) step **(B)**. A CS step only weakens the overall
843 affinity compared to the equilibrium constant of the physical binding step (K_2 ; 14 μM for
844 Danusertib, see Figure 5), whereas an IF step makes the binding tighter. **(C)** Effect on the
845 overall K_D for Danusertib when changing the equilibrium constants K_1 and K_2 by two orders of
846 magnitude starting from their actual values (see Figure 5I).

847
848 **Figure 7.** Mechanism of AT9283 drug binding to Aurora A at 25 °C. **(A)** The increase in
849 fluorescence at 25 °C upon AT9283 binding fitted to a double exponential. **(B)** The plot of
850 $k_{obs,Binding}$ versus AT9283 concentration for the fast phase yields $k_2 = 3.4 \pm 0.5 \mu\text{M}^{-1}\text{s}^{-1}$ and an

851 underdetermined intercept (k_{-2}) and **(C)** the k_{obs} of the slow phase reaches a plateau around
852 $0.8 \pm 0.2 \text{ s}^{-1}$. **(D)** Dilution of the Aurora A/AT9283 complex formed after 1 hour of incubation.
853 The slow dissociation was measured by Creoptix WAVE waveguide interferometry and fitted
854 with a double exponential with rate constants of $(1.1 \pm 0.02) \times 10^{-2} \text{ s}^{-1}$ and $(0.1 \pm 0.01) \times 10^{-2} \text{ s}^{-1}$.
855 **(E)** Double-jump experiments (1 s incubation time of 1 μM AT9283 to Aurora A followed by 60 s
856 long dissociation step initiated by a wash with buffer) was measured by Creoptix WAVE
857 waveguide interferometry to properly define the value of $k_{-2} = (1.0 \pm 0.1) \times 10^{-2} \text{ s}^{-1}$. **(F)**
858 Macroscopic dissociation constant (K_D) determined by Creoptix WAVE waveguide
859 interferometry: surface-immobilized Aurora A was incubated with various concentration of
860 AT9283 (0.03 nM (black), 0.27 nM (blue), 0.8 nM (purple), 2.4 nM (green), 7.2 nM (red), 21.6
861 nM (cyan), and 64.8 nM (orange)) and surface mass accumulation was observed until
862 establishment of equilibrium. **(G)** A plot of the final equilibrium value versus AT9283
863 concentration yields a $K_D = 2.1 \pm 1.8 \text{ nM}$. **(H)** Binding scheme for AT9283 (labeled AT)
864 highlighting a four-steps binding mechanism, that contains binding to two different states, a
865 conformational selection mechanism and an induced-fit step. Kinetic constants shown in H were
866 determined from global fitting (see Figure 8). Fluorescence traces are the average of at least
867 five replicate measurements ($n > 5$), and error bars and uncertainties given in B, C, G and H
868 denote the (propagated) standard deviation in the fitted parameter.

869
870 **Figure 7-figure supplement 1. (A)** Kinetic partitioning of Aurora A with AT9283. The apparent
871 discrepancy between the experimentally observed off rates and the microscopic rate constant,
872 k_{-3} , can be explained by considering the kinetic partitioning. **(B)** Double-jump experiments
873 measured by Creoptix WAVE waveguide interferometry at 25 °C of AT9283 at 1 and 3 s
874 incubation time before induction of dissociation by a buffer wash are best described with a
875 single exponential function of ($k = 0.01 \text{ s}^{-1}$). Uncertainties given in A denote the (propagated)
876 standard deviation in the fitted parameter.

877
878 **Figure 8.** Global fits of AT9283 binding and dissociation kinetics to Aurora A at 25 °C. Binding
879 kinetics was monitored by stopped-flow fluorescence at different concentrations of AT9283
880 (indicated) to 0.5 μM Aurora A. Dissociation kinetics were obtained for fully equilibrated
881 drug/kinase complex (k_{off}^{obs}) or for the initial encounter complex (k_{off}^{djump}) by using a 1 hour or a
882 short 2 s incubation of the kinase with AT9283, respectively, before inducing dissociation by a
883 buffer wash using Creoptix WAVE waveguide interferometry. Global fitting was performed with

884 KinTek Explorer software using the model in Figure 7H (reduced $\chi^2 = 3.2$). Fluorescence traces
885 are the average of at least five replicate measurements ($n > 5$).

886
887 **Figure 8-figure supplement 1.** Alternative binding models of AT9283 to Aurora A cannot
888 explain the experimental data. **(A)** Our initial three-state binding scheme, where AT9283 binds
889 only the DFG_{in} state of Aurora A and is followed by an induced-fit step, is incorrect. The best
890 global fit (shown in red) did not describe the data as can be seen by visual inspection and from
891 the reduced χ^2 value of 36. **(B)** An alternative model, where AT9283 can bind to Aurora A
892 irrespective of the state of the DFG-loop, and binding is followed by an induced-fit step did not
893 result in adequate fits (data not shown) and yield a reduced χ^2 value of 52. In both cases the
894 values for the interconversion between AurA_{out} and AurA_{in} were taken from the Gleevec
895 experiment (Figure 5-figure supplement 2). Fluorescence traces are the average of at least five
896 replicate measurements ($n > 5$).

897
898 **Figure 9.** X-ray structures of Aurora A bound to inhibitor AT9283 reveal multiple binding modes.
899 **(A)** AT9283 (pink) bound to the active site of Aurora A (PDB 2W1G, (Howard et al., 2009))
900 shows the DFG_{in}-loop conformation and a salt bridge between K162 and E181. **(B)** Aurora A
901 dimer (light and dark blue ribbon) in complex with AT9283 (pink) and inhibiting monobody (Mb,
902 grey), showing DFG_{out}-loop and broken K162 and E181 salt bridge (PDB 6CPG).

903
904 **Figure 10.** Mechanism of ATP binding to Aurora A at 10 °C. **(A)** Binding of mant-ATP to Aurora
905 A was followed by an increase in fluorescence with biphasic kinetics. The plot of k_{obs} versus
906 concentration of mant-ATP of the fast phase **(B)** yields $k_2 = 0.8 \pm 0.2 \mu\text{M}^{-1}\text{s}^{-1}$ and $k_{-2} = 50 \pm 8 \text{ s}^{-1}$
907 and the slow phase **(C)** reached a plateau around $21 \pm 1 \text{ s}^{-1}$ ($k_3 + k_{-3}$). **(D)** Dissociation
908 kinetics of 10 μM Aurora A/10 μM mant-ATP complex was measured after a 11-fold dilution into
909 buffer and yields $k_{off}^{obs} = 17.2 \pm 1 \text{ s}^{-1}$. **(E, F)** Macroscopic dissociation constant of Aurora A with
910 mant-ATP measured by fluorescence energy transfer. **(E)** Emission spectra (excitation at 290
911 nm) of 1 μM Aurora A (green), 160 μM mant-ATP (red), and 1 μM Aurora A/160 μM mant-ATP
912 (blue). **(F)** The change in fluorescence at 450 nm (ΔF^{450}) versus mant-ATP concentrations yields
913 $K_D = 22 \pm 6 \mu\text{M}$. **(G)** Global fitting (red) of all kinetics data (black) in KinTek Explorer to the
914 binding scheme shown in **(H)** results in the kinetic constants given in the scheme and an overall
915 $K_D = 48 \pm 8 \mu\text{M}$, calculated from all rate constants. Fluorescence traces are the average of at

916 least five replicate measurements ($n > 5$), and error bars and uncertainties given in B, C, D, F,
 917 and H denote the (propagated) standard deviation in the fitted parameter.

918

919

920 **Table 1** Data collection and refinement statistics for dephosphorylated Aurora A (122-403)

921

922

	apo-Aurora A (6CPE)	Aurora A + AMPPCP (6CPF)	Aurora A + Mb + AT9283 (6CPG)
Data collection			
Space group	P 61 2 2	P 61 2 2	P 21 21 21
Cell dimensions			
<i>a</i> , <i>b</i> , <i>c</i> (Å)	80.55, 80.55, 169.79	81.75, 81.75, 172.87	63.86, 69.7, 175.56
α , β , γ (°)	90, 90, 120	90, 90, 120	90, 90, 90
Resolution (Å)	84.90 – 2.45 (2.55 – 2.45) ^a	86.44 – 2.30 (2.39 – 2.30) ^a	43.14 – 2.80 (2.87 – 2.80) ^a
<i>R</i> _{meas}	0.073 (1.308)	0.113 (2.260)	0.189 (1.268)
<i>I</i> / σ (<i>I</i>)	15.0 (1.6)	10.3 (1.3)	8.9 (1.1)
<i>CC</i> _{1/2}	0.998 (0.711)	0.997 (0.465)	0.986 (0.625)
Completeness (%)	99.9 (100)	100 (100)	99.2 (98.8)
Redundancy	7.6 (6.3)	9.7 (7.8)	5.4 (5.3)
Refinement			
Resolution (Å)	64.52 – 2.45	54.79 – 2.30	36.17 – 2.80
No. reflections	12617 (1224)	15756 (1527)	19556 (1845)
<i>R</i> _{work} / <i>R</i> _{free}	0.2151 / 0.2528	0.2179 / 0.2587	0.2792 / 0.3350
No. atoms			
Protein	2035	2055	5122
Ligand/ion	11	32	56
Water	4	6	
<i>B</i> factors			
Protein	71.83	63.68	78.84
Ligand/ion	75.77	76.44	81.05
Water	52.52	45.84	
R.m.s. deviations			
Bond lengths (Å)	0.005	0.004	0.003
Bond angles (°)	0.98	0.97	0.98

923 The number of crystals for each structure is 1 for apo-Aurora A and Aurora A + AMPPCP and 2 crystals
 924 for Aurora A + Mb + AT9283.

925 ^a Values in parentheses are for highest-resolution shell.

926

927

928

929

930

References

931

932 Adams, P. D., Afonine, P. V., Bunkoczi, G., Chen, V. B., Davis, I. W., Echols, N., . . . Zwart, P. H.
 933 (2010). PHENIX: a comprehensive Python-based system for macromolecular

934 structure solution. *Acta Crystallogr D Biol Crystallogr*, 66(Pt 2), 213-221.
935 doi:10.1107/S0907444909052925

936 Afonine, P. V., Grosse-Kunstleve, R. W., Echols, N., Headd, J. J., Moriarty, N. W., Mustyakimov,
937 M., . . . Adams, P. D. (2012). Towards automated crystallographic structure
938 refinement with phenix.refine. *Acta Crystallogr D Biol Crystallogr*, 68(Pt 4), 352-367.
939 doi:10.1107/S0907444912001308

940 Agafonov, R. V., Wilson, C., Otten, R., Buosi, V., & Kern, D. (2014). Energetic dissection of
941 Gleevec's selectivity toward human tyrosine kinases. *Nat Struct Mol Biol*, 21(10),
942 848-853. doi:10.1038/nsmb.2891

943 Asteriti, I. A., Daidone, F., Colotti, G., Rinaldo, S., Lavia, P., Guarguaglini, G., & Paiardini, A.
944 (2017). Identification of small molecule inhibitors of the Aurora-A/TPX2 complex.
945 *Oncotarget*, 8(19), 32117-32133. doi:10.18632/oncotarget.16738

946 Badrinarayan, P., & Sastry, G. N. (2014). Specificity rendering 'hot-spots' for aurora kinase
947 inhibitor design: the role of non-covalent interactions and conformational
948 transitions. *PLoS One*, 9(12), e113773. doi:10.1371/journal.pone.0113773

949 Barakat, K. H., Huzil, J. T., Jordan, K. E., Evangelinos, C., Houghton, M., & Tuszynski, J. (2013).
950 A computational model for overcoming drug resistance using selective dual-
951 inhibitors for aurora kinase A and its T217D variant. *Mol Pharm*, 10(12), 4572-4589.
952 doi:10.1021/mp4003893

953 Battye, T. G., Kontogiannis, L., Johnson, O., Powell, H. R., & Leslie, A. G. (2011). iMOSFLM: a
954 new graphical interface for diffraction-image processing with MOSFLM. *Acta*
955 *Crystallogr D Biol Crystallogr*, 67(Pt 4), 271-281. doi:10.1107/S0907444910048675

956 Bavetsias, V., & Linardopoulos, S. (2015). Aurora Kinase Inhibitors: Current Status and
957 Outlook. *Front Oncol*, 5, 278. doi:10.3389/fonc.2015.00278

958 Bavetsias, V., Perez-Fuertes, Y., McIntyre, P. J., Atrash, B., Kosmopoulou, M., O'Fee, L., . . .
959 Blagg, J. (2015). 7-(Pyrazol-4-yl)-3H-imidazo[4,5-b]pyridine-based derivatives for
960 kinase inhibition: Co-crystallisation studies with Aurora-A reveal distinct
961 differences in the orientation of the pyrazole N1-substituent. *Bioorg Med Chem Lett*,
962 25(19), 4203-4209. doi:10.1016/j.bmcl.2015.08.003

963 Bayliss, R., Burgess, S. G., & McIntyre, P. J. (2017). Switching Aurora-A kinase on and off at
964 an allosteric site. *FEBS J*, 284(18), 2947-2954. doi:10.1111/febs.14069

965 Bayliss, R., Sardon, T., Vernos, I., & Conti, E. (2003). Structural basis of Aurora-A activation
966 by TPX2 at the mitotic spindle. *Molecular Cell*, 12(4), 851-862. doi:10.1016/S1097-2765(03)00392-7

967 Berezov, A., Zhang, H. T., Greene, M. I., & Murali, R. (2001). Disabling erbB receptors with
968 rationally designed exocyclic mimetics of antibodies: structure-function analysis. *J*
969 *Med Chem*, 44(16), 2565-2574.

970 Borisa, A. C., & Bhatt, H. G. (2017). A comprehensive review on Aurora kinase: Small
971 molecule inhibitors and clinical trial studies. *Eur J Med Chem*, 140, 1-19.
972 doi:10.1016/j.ejmech.2017.08.045

973 Burgess, S. G., Oleksy, A., Cavazza, T., Richards, M. W., Vernos, I., Matthews, D., & Bayliss, R.
974 (2016). Allosteric inhibition of Aurora-A kinase by a synthetic vNAR domain. *Open*
975 *Biol*, 6(7). doi:10.1098/rsob.160089

976 Campos-Olivas, R., Marenchino, M., Scapozza, L., & Gervasio, F. L. (2011). Backbone
977 assignment of the tyrosine kinase Src catalytic domain in complex with imatinib.
978 *Biomol NMR Assign*, 5(2), 221-224. doi:10.1007/s12104-011-9304-7

979

980 Carpinelli, P., Ceruti, R., Giorgini, M. L., Cappella, P., Gianellini, L., Croci, V., . . . Moll, J. (2007).
981 PHA-739358, a potent inhibitor of Aurora kinases with a selective target inhibition
982 profile relevant to cancer. *Mol Cancer Ther*, 6(12 Pt 1), 3158-3168.
983 doi:10.1158/1535-7163.MCT-07-0444

984 Carvajal, R. D., Tse, A., & Schwartz, G. K. (2006). Aurora kinases: new targets for cancer
985 therapy. *Clin Cancer Res*, 12(23), 6869-6875. doi:10.1158/1078-0432.CCR-06-1405

986 Cheetham, G. M., Knechtel, R. M., Coll, J. T., Renwick, S. B., Swenson, L., Weber, P., . . . Austen,
987 D. A. (2002). Crystal structure of aurora-2, an oncogenic serine/threonine kinase. *J*
988 *Biol Chem*, 277(45), 42419-42422. doi:10.1074/jbc.C200426200

989 Chen, C., Ha, B. H., Thevenin, A. F., Lou, H. J., Zhang, R., Yip, K. Y., . . . Turk, B. E. (2014).
990 Identification of a major determinant for serine-threonine kinase phosphoacceptor
991 specificity. *Molecular Cell*, 53(1), 140-147. doi:10.1016/j.molcel.2013.11.013

992 Chen, V. B., Arendall, W. B., 3rd, Headd, J. J., Keedy, D. A., Immormino, R. M., Kapral, G. J., . . .
993 Richardson, D. C. (2010). MolProbity: all-atom structure validation for
994 macromolecular crystallography. *Acta Crystallogr D Biol Crystallogr*, 66(Pt 1), 12-21.
995 doi:10.1107/S0907444909042073

996 Cohen, P. (2002). Protein kinases - the major drug targets of the twenty-first century?
997 *Nature Reviews Drug Discovery*, 1(4), 309-315. doi:10.1038/nrd773

998 Copeland, R. A. (2016). The drug-target residence time model: a 10-year retrospective.
999 *Nature Reviews Drug Discovery*, 15(2), 87-95. doi:10.1038/nrd.2015.18

1000 Copeland, R. A., Pompliano, D. L., & Meek, T. D. (2006). Drug-target residence time and its
1001 implications for lead optimization. *Nature Reviews Drug Discovery*, 5(9), 730-739.
1002 doi:10.1038/nrd2082

1003 Crowley, P. B., Kyne, C., & Monteith, W. B. (2012). Simple and inexpensive incorporation of
1004 19F-tryptophan for protein NMR spectroscopy. *Chem Commun (Camb)*, 48(86),
1005 10681-10683. doi:10.1039/c2cc35347d

1006 Cyphers, S., Ruff, E. F., Behr, J. M., Chodera, J. D., & Levinson, N. M. (2017). A water-mediated
1007 allosteric network governs activation of Aurora kinase A. *Nat Chem Biol*, 13(4), 402-
1008 408. doi:10.1038/nchembio.2296

1009 Dar, A. C., Lopez, M. S., & Shokat, K. M. (2008). Small molecule recognition of c-Src via the
1010 Imatinib-binding conformation. *Chem Biol*, 15(10), 1015-1022.
1011 doi:10.1016/j.chembiol.2008.09.007

1012 Delaglio, F., Grzesiek, S., Vuister, G. W., Zhu, G., Pfeifer, J., & Bax, A. (1995). NMRPipe: a
1013 multidimensional spectral processing system based on UNIX pipes. *J Biomol NMR*,
1014 6(3), 277-293.

1015 DiMaio, F., Echols, N., Headd, J. J., Terwilliger, T. C., Adams, P. D., & Baker, D. (2013).
1016 Improved low-resolution crystallographic refinement with Phenix and Rosetta. *Nat*
1017 *Methods*, 10(11), 1102-1104. doi:10.1038/nmeth.2648

1018 Dodson, C. A., Kosmopoulou, M., Richards, M. W., Atrash, B., Bavetsias, V., Blagg, J., & Bayliss,
1019 R. (2010). Crystal structure of an Aurora-A mutant that mimics Aurora-B bound to
1020 MLN8054: insights into selectivity and drug design. *Biochemical Journal*, 427, 19-28.
1021 doi:10.1042/Bj20091530

1022 Emsley, P., & Cowtan, K. (2004). Coot: model-building tools for molecular graphics. *Acta*
1023 *Crystallogr D Biol Crystallogr*, 60(Pt 12 Pt 1), 2126-2132.
1024 doi:10.1107/S0907444904019158

1025 Emsley, P., Lohkamp, B., Scott, W. G., & Cowtan, K. (2010). Features and development of
1026 Coot. *Acta Crystallogr D Biol Crystallogr*, 66(Pt 4), 486-501.
1027 doi:10.1107/S0907444910007493

1028 Evans, P. R., & Murshudov, G. N. (2013). How good are my data and what is the resolution?
1029 *Acta Crystallogr D Biol Crystallogr*, 69(Pt 7), 1204-1214.
1030 doi:10.1107/S0907444913000061

1031 Fancelli, D., Moll, J., Varasi, M., Bravo, R., Artico, R., Berta, D., . . . Vianello, P. (2006). 1,4,5,6-
1032 tetrahydropyrrolo[3,4-c]pyrazoles: identification of a potent Aurora kinase inhibitor
1033 with a favorable antitumor kinase inhibition profile. *J Med Chem*, 49(24), 7247-7251.
1034 doi:10.1021/jm060897w

1035 Ferguson, F. M., Doctor, Z. M., Chaikuad, A., Sim, T., Kim, N. D., Knapp, S., & Gray, N. S. (2017).
1036 Characterization of a highly selective inhibitor of the Aurora kinases. *Bioorg Med*
1037 *Chem Lett*, 27(18), 4405-4408. doi:10.1016/j.bmcl.2017.08.016

1038 Fraedrich, K., Schrader, J., Itrich, H., Keller, G., Gontarewicz, A., Matzat, V., . . . Benten, D.
1039 (2012). Targeting Aurora Kinases with Danusertib (PHA-739358) Inhibits Growth of
1040 Liver Metastases from Gastroenteropancreatic Neuroendocrine Tumors in an
1041 Orthotopic Xenograft Model. *Clinical Cancer Research*, 18(17), 4621-4632.
1042 doi:10.1158/1078-0432.Ccr-11-2968

1043 Fu, J. Y., Bian, M. L., Jiang, Q., & Zhang, C. M. (2007). Roles of aurora kinases in mitosis and
1044 tumorigenesis. *Molecular Cancer Research*, 5(1), 1-10. doi:10.1158/1541-7786.Mcr-
1045 06-0208

1046 Gautschi, O., Heighway, J., Mack, P. C., Purnell, P. R., Lara, P. N., & Gandara, D. R. (2008).
1047 Aurora kinases as anticancer drug targets. *Clinical Cancer Research*, 14(6), 1639-
1048 1648. doi:10.1158/1078-0432.Ccr-07-2179

1049 Gilbert, J. A. H., Sarkar, H., Sheldrake, P., Blagg, J., Ying, L., & Dodson, C. A. (2017). Dynamic
1050 Equilibrium of the Aurora A Kinase Activation Loop Revealed by Single-Molecule
1051 Spectroscopy. *Angew Chem Int Ed Engl*, 56(38), 11409-11414.
1052 doi:10.1002/anie.201704654

1053 Goddard, T. D. K., D.G. (2008). SPARKY 3 (Version 3.115). San Francisco: University of
1054 California.

1055 Gustafson, W. C., Meyerowitz, J. G., Nekritz, E. A., Chen, J., Benes, C., Charron, E., . . . Weiss, W.
1056 A. (2014). Drugging MYCN through an allosteric transition in Aurora kinase A. *Cancer Cell*, 26(3), 414-427. doi:10.1016/j.ccr.2014.07.015

1057 Helmus, J. J., & Jaroniec, C. P. (2013). Nmrglue: an open source Python package for the
1058 analysis of multidimensional NMR data. *J Biomol NMR*, 55(4), 355-367.
1059 doi:10.1007/s10858-013-9718-x

1060 Heron, N. M., Anderson, M., Blowers, D. P., Breed, J., Eden, J. M., Green, S., . . . Rowsell, S.
1061 (2006). SAR and inhibitor complex structure determination of a novel class of
1062 potent and specific Aurora kinase inhibitors. *Bioorg Med Chem Lett*, 16(5), 1320-
1063 1323. doi:10.1016/j.bmcl.2005.11.053

1064 Hopkins, A. L., & Groom, C. R. (2002). The druggable genome. *Nature Reviews Drug*
1065 *Discovery*, 1(9), 727-730. doi:10.1038/nrd892

1066 Howard, S., Berdini, V., Boulstridge, J. A., Carr, M. G., Cross, D. M., Curry, J., . . . Wyatt, P. G.
1067 (2009). Fragment-based discovery of the pyrazol-4-yl urea (AT9283), a
1068 multitargeted kinase inhibitor with potent aurora kinase activity. *J Med Chem*, 52(2),
1069 379-388. doi:10.1021/jm800984v

1070

1071 Iqbal, N., & Iqbal, N. (2014). Imatinib: a breakthrough of targeted therapy in cancer.
1072 *Chemother Res Pract*, 2014, 357027. doi:10.1155/2014/357027

1073 Janecek, M., Rossmann, M., Sharma, P., Emery, A., Huggins, D. J., Stockwell, S. R., . . .
1074 Venkitaraman, A. R. (2016). Allosteric modulation of AURKA kinase activity by a
1075 small-molecule inhibitor of its protein-protein interaction with TPX2. *Sci Rep*, 6,
1076 28528. doi:10.1038/srep28528

1077 Johnson, K. A. (2009). Fitting enzyme kinetic data with KinTek Global Kinetic Explorer.
1078 *Methods Enzymol*, 467, 601-626. doi:10.1016/S0076-6879(09)67023-3

1079 Johnson, K. A., Simpson, Z. B., & Blom, T. (2009). Global Kinetic Explorer: A new computer
1080 program for dynamic simulation and fitting of kinetic data. *Analytical Biochemistry*,
1081 387(1), 20-29. doi:10.1016/j.ab.2008.12.024

1082 Kabsch, W. (2010). Xds. *Acta Crystallogr D Biol Crystallogr*, 66(Pt 2), 125-132.
1083 doi:10.1107/S0907444909047337

1084 Katayama, H., & Sen, S. (2010). Aurora kinase inhibitors as anticancer molecules.
1085 *Biochimica Et Biophysica Acta-Gene Regulatory Mechanisms*, 1799(10-12), 829-839.
1086 doi:10.1016/j.bbagr.2010.09.004

1087 Kilchmann, F., Marcaida, M. J., Kotak, S., Schick, T., Boss, S. D., Awale, M., . . . Reymond, J. L.
1088 (2016). Discovery of a Selective Aurora A Kinase Inhibitor by Virtual Screening. *J*
1089 *Med Chem*, 59(15), 7188-7211. doi:10.1021/acs.jmedchem.6b00709

1090 Kitevski-LeBlanc, J. L., & Prosser, R. S. (2012). Current applications of 19F NMR to studies of
1091 protein structure and dynamics. *Prog Nucl Magn Reson Spectrosc*, 62, 1-33.
1092 doi:10.1016/j.pnmrs.2011.06.003

1093 Kollareddy, M., Zheleva, D., Dzubak, P., Brahmakshatriya, P. S., Lepsik, M., & Hajdich, M.
1094 (2012). Aurora kinase inhibitors: progress towards the clinic. *Invest New Drugs*,
1095 30(6), 2411-2432. doi:10.1007/s10637-012-9798-6

1096 Kornev, A. P., & Taylor, S. S. (2010). Defining the conserved internal architecture of a
1097 protein kinase. *Biochimica Et Biophysica Acta-Proteins and Proteomics*, 1804(3), 440-
1098 444. doi:10.1016/j.bbapap.2009.10.017

1099 Kornev, A. P., & Taylor, S. S. (2015). Dynamics-Driven Allostery in Protein Kinases. *Trends*
1100 *Biochem Sci*, 40(11), 628-647. doi:10.1016/j.tibs.2015.09.002

1101 Kowiel, M., Jaskolski, M., & Dauter, Z. (2014). ACHESYM: an algorithm and server for
1102 standardized placement of macromolecular models in the unit cell. *Acta Crystallogr*
1103 *D Biol Crystallogr*, 70(Pt 12), 3290-3298. doi:10.1107/S1399004714024572

1104 Langer, T., Vogtherr, M., Elshorst, B., Betz, M., Schieberr, U., Saxena, K., & Schwalbe, H.
1105 (2004). NMR backbone assignment of a protein kinase catalytic domain by a
1106 combination of several approaches: application to the catalytic subunit of cAMP-
1107 dependent protein kinase. *Chembiochem*, 5(11), 1508-1516.
1108 doi:10.1002/cbic.200400129

1109 Lemaire, P. A., Tessmer, I., Craig, R., Erie, D. A., & Cole, J. L. (2006). Unactivated PKR exists in
1110 an open conformation capable of binding nucleotides. *Biochemistry*, 45(30), 9074-
1111 9084. doi:10.1021/bi060567d

1112 Levinson, N. M., Kuchment, O., Shen, K., Young, M. A., Koldobskiy, M., Karplus, M., . . .
1113 Kuriyan, J. (2006). A Src-like inactive conformation in the abl tyrosine kinase
1114 domain. *PLoS Biol*, 4(5), e144. doi:10.1371/journal.pbio.0040144

1115 Liu, Y., & Gray, N. S. (2006). Rational design of inhibitors that bind to inactive kinase
1116 conformations. *Nat Chem Biol*, 2(7), 358-364. doi:10.1038/nchembio799

1117 Lok, W., Klein, R. Q., & Saif, M. W. (2010). Aurora kinase inhibitors as anti-cancer therapy.
1118 *Anticancer Drugs*, 21(4), 339-350. doi:10.1097/CAD.0b013e3283350dd1

1119 Lovera, S., Sutto, L., Boubeva, R., Scapozza, L., Dolker, N., & Gervasio, F. L. (2012). The
1120 different flexibility of c-Src and c-Abl kinases regulates the accessibility of a
1121 druggable inactive conformation. *J Am Chem Soc*, 134(5), 2496-2499.
1122 doi:10.1021/ja210751t

1123 Lukasiewicz, K. B., & Lingle, W. L. (2009). Aurora A, centrosome structure, and the
1124 centrosome cycle. *Environ Mol Mutagen*, 50(8), 602-619. doi:10.1002/em.20533

1125 Martin, M. P., Zhu, J. Y., Lawrence, H. R., Pireddu, R., Luo, Y., Alam, R., . . . Schonbrunn, E.
1126 (2012). A novel mechanism by which small molecule inhibitors induce the DFG flip
1127 in Aurora A. *ACS Chem Biol*, 7(4), 698-706. doi:10.1021/cb200508b

1128 Marumoto, T., Zhang, D. W., & Saya, H. (2005). Aurora-A - A guardian of poles. *Nature*
1129 *Reviews Cancer*, 5(1), 42-50. doi:10.1038/nrc1526

1130 Marzo, I., & Naval, J. (2013). Antimitotic drugs in cancer chemotherapy: Promises and
1131 pitfalls. *Biochemical Pharmacology*, 86(6), 703-710. doi:10.1016/j.bcp.2013.07.010

1132 McCoy, A. J., Grosse-Kunstleve, R. W., Adams, P. D., Winn, M. D., Storoni, L. C., & Read, R. J.
1133 (2007). Phaser crystallographic software. *Journal of Applied Crystallography*, 40(Pt
1134 4), 658-674. doi:10.1107/S0021889807021206

1135 McIntyre, P. J., Collins, P. M., Vrzal, L., Birchall, K., Arnold, L. H., Mpamhanga, C., . . . Bayliss, R.
1136 (2017). Characterization of Three Druggable Hot-Spots in the Aurora-A/TPX2
1137 Interaction Using Biochemical, Biophysical, and Fragment-Based Approaches. *ACS*
1138 *Chem Biol*, 12(11), 2906-2914. doi:10.1021/acscchembio.7b00537

1139 Meng, Y., Lin, Y. L., & Roux, B. (2015). Computational study of the "DFG-flip" conformational
1140 transition in c-Abl and c-Src tyrosine kinases. *J Phys Chem B*, 119(4), 1443-1456.
1141 doi:10.1021/jp511792a

1142 Meng, Y., Pond, M. P., & Roux, B. (2017). Tyrosine Kinase Activation and Conformational
1143 Flexibility: Lessons from Src-Family Tyrosine Kinases. *Acc Chem Res*, 50(5), 1193-
1144 1201. doi:10.1021/acs.accounts.7b00012

1145 Nagar, B., Bornmann, W. G., Pellicena, P., Schindler, T., Veach, D. R., Miller, W. T., . . . Kuriyan,
1146 J. (2002). Crystal structures of the kinase domain of c-Abl in complex with the small
1147 molecule inhibitors PD173955 and imatinib (STI-571). *Cancer Res*, 62(15), 4236-
1148 4243.

1149 Ni, Q., Shaffer, J., & Adams, J. A. (2000). Insights into nucleotide binding in protein kinase A
1150 using fluorescent adenosine derivatives. *Protein Sci*, 9(9), 1818-1827.
1151 doi:10.1110/ps.9.9.1818

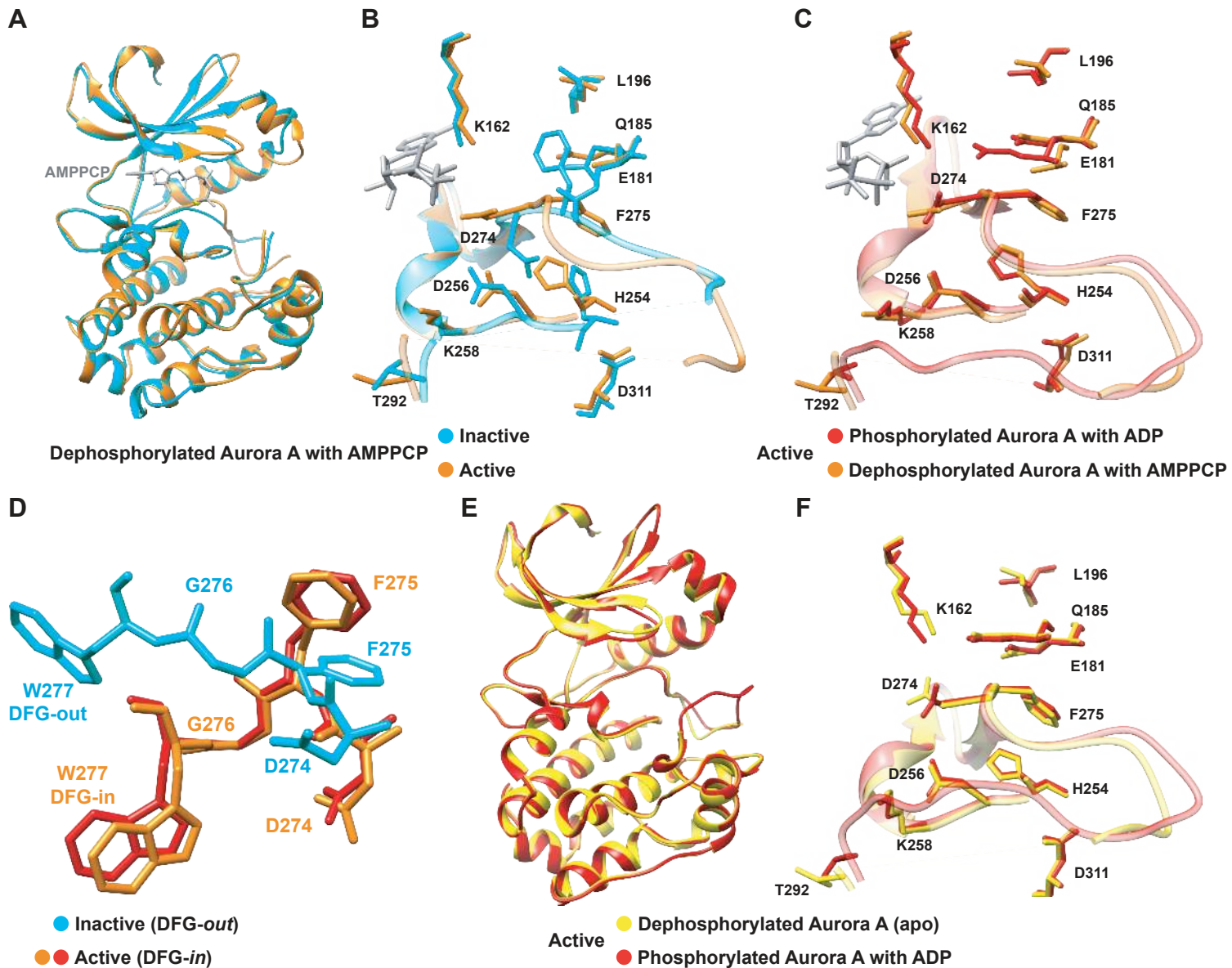
1152 Nikonova, A. S., Astsaturrov, I., Serebriiskii, I. G., Dunbrack, R. L., Jr., & Golemis, E. A. (2013).
1153 Aurora A kinase (AURKA) in normal and pathological cell division. *Cell Mol Life Sci*,
1154 70(4), 661-687. doi:10.1007/s00018-012-1073-7

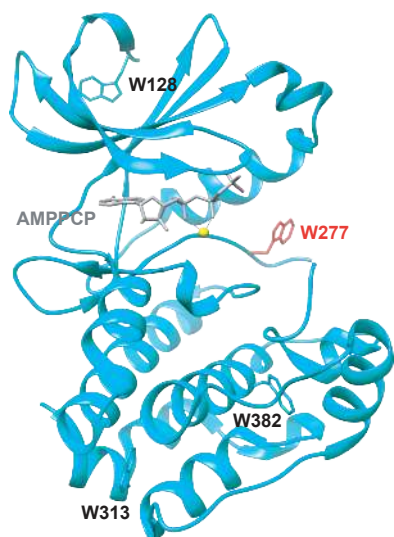
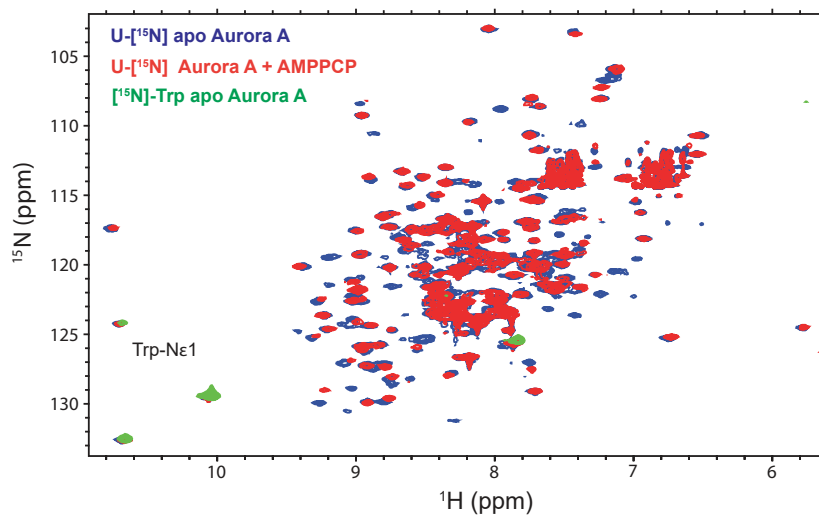
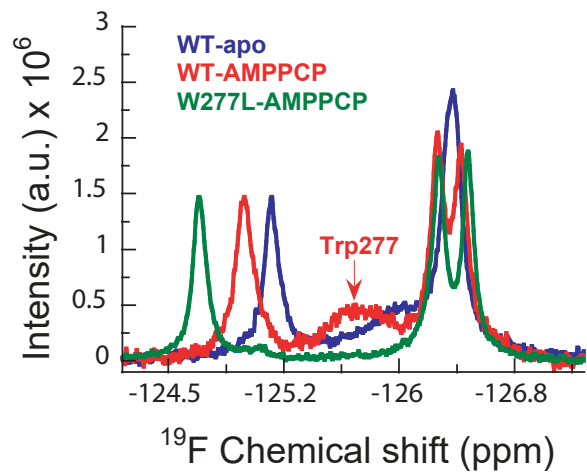
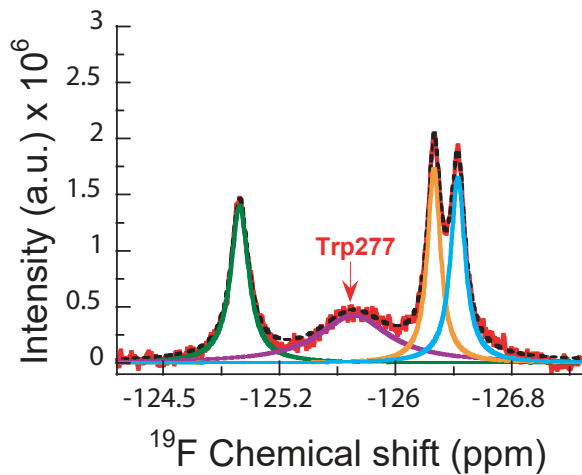
1155 Nowakowski, J., Cronin, C. N., McRee, D. E., Knuth, M. W., Nelson, C. G., Pavletich, N. P., . . .
1156 Thompson, D. A. (2002). Structures of the cancer-related Aurora-A, FAK, and EphA2
1157 protein kinases from nanovolume crystallography. *Structure*, 10(12), 1659-1667.

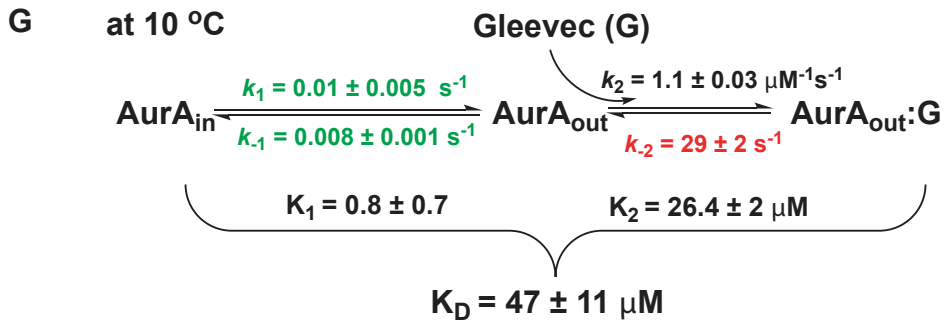
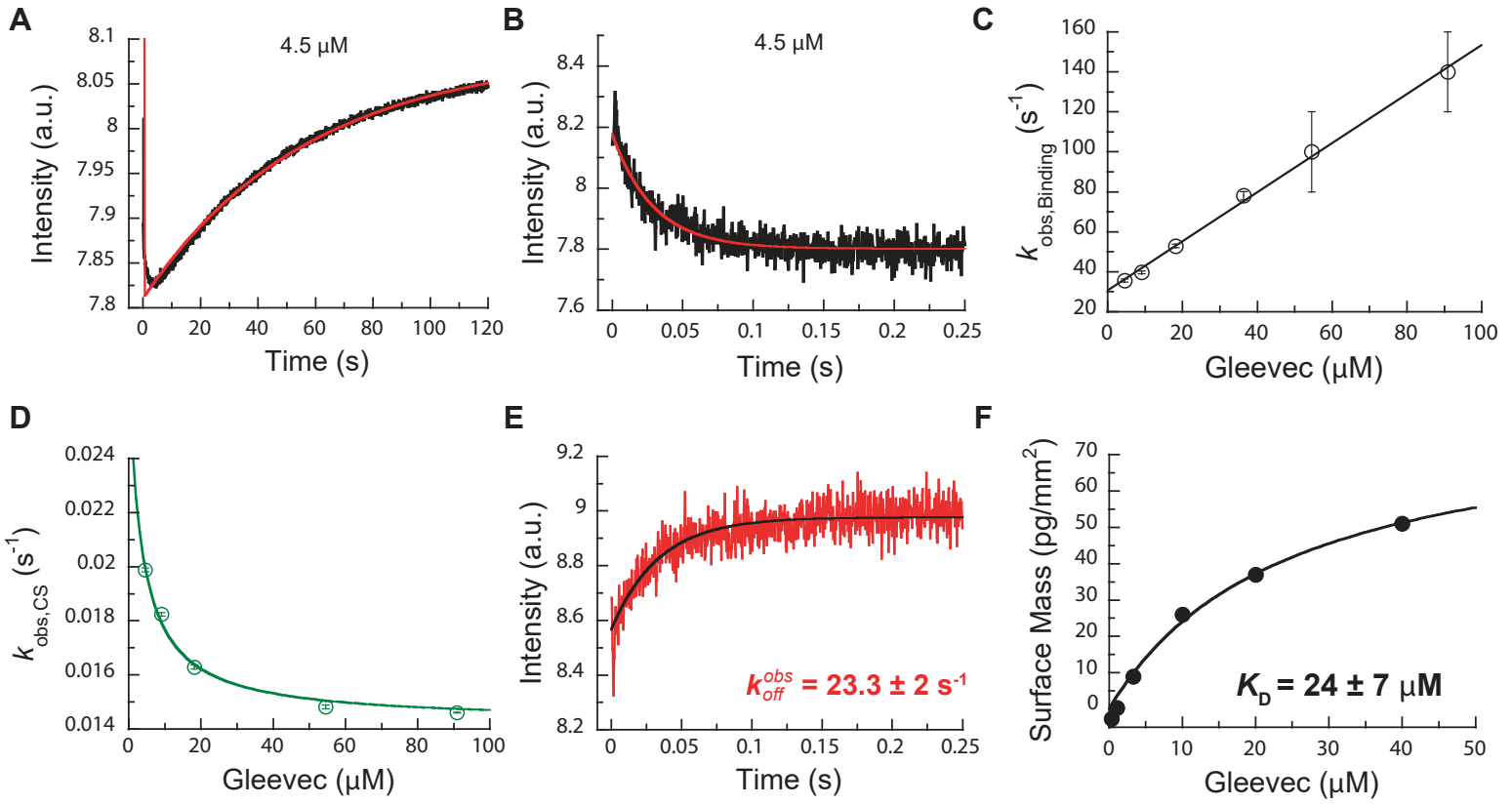
1158 Pettersen, E. F., Goddard, T. D., Huang, C. C., Couch, G. S., Greenblatt, D. M., Meng, E. C., &
1159 Ferrin, T. E. (2004). UCSF Chimera--a visualization system for exploratory research
1160 and analysis. *J Comput Chem*, 25(13), 1605-1612. doi:10.1002/jcc.20084

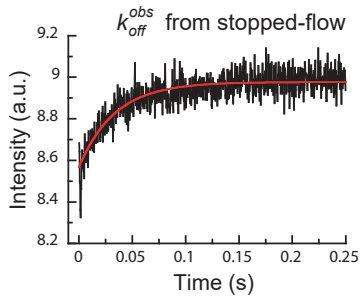
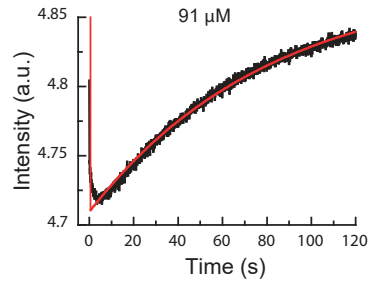
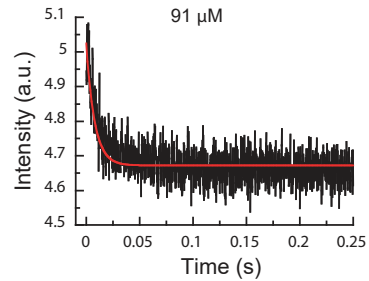
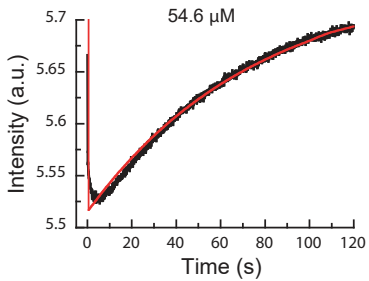
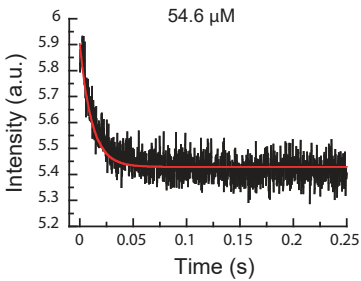
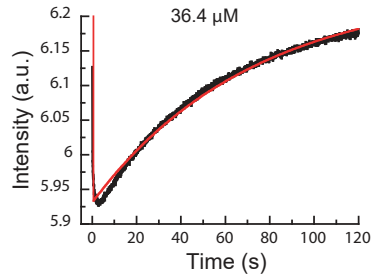
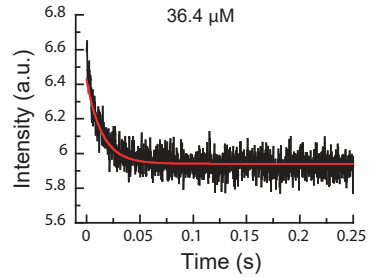
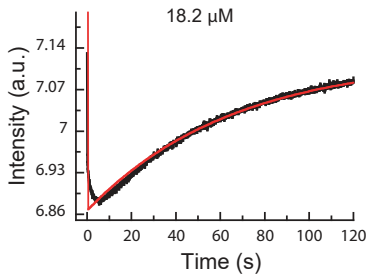
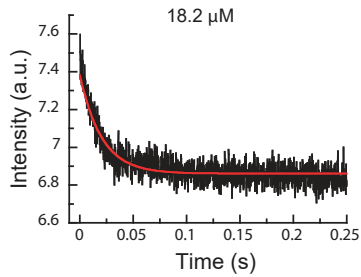
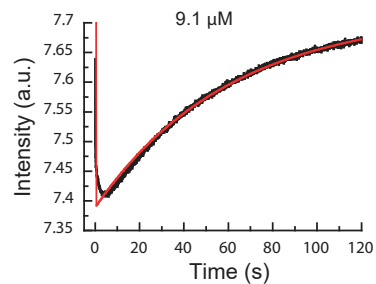
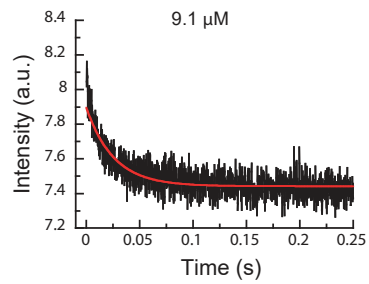
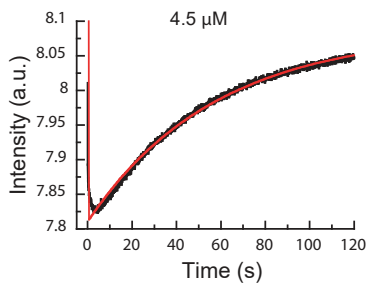
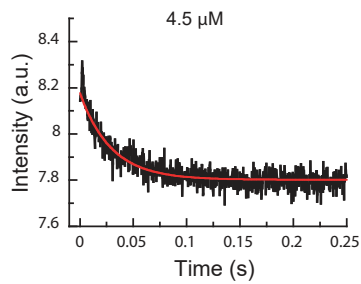
1161 Ruff, E. F., Muretta, J. M., Thompson, A. R., Lake, E. W., Cyphers, S., Albanese, S. K., . . .
1162 Levinson, N. M. (2018). A dynamic mechanism for allosteric activation of Aurora
1163 kinase A by activation loop phosphorylation. *Elife*, 7. doi:10.7554/eLife.32766
1164 Sarvagalla, S., & Coumar, M. S. (2015). Structural Biology Insight for the Design of Sub-type
1165 Selective Aurora Kinase Inhibitors. *Curr Cancer Drug Targets*, 15(5), 375-393.
1166 Schindler, T., Bornmann, W., Pellicena, P., Miller, W. T., Clarkson, B., & Kuriyan, J. (2000).
1167 Structural mechanism for STI-571 inhibition of abelson tyrosine kinase. *Science*,
1168 289(5486), 1938-1942.
1169 Schneider, E. V., Bottcher, J., Huber, R., Maskos, K., & Neumann, L. (2013). Structure-kinetic
1170 relationship study of CDK8/CycC specific compounds. *Proc Natl Acad Sci U S A*,
1171 110(20), 8081-8086. doi:10.1073/pnas.1305378110
1172 Seeliger, M. A., Nagar, B., Frank, F., Cao, X., Henderson, M. N., & Kuriyan, J. (2007). c-Src
1173 binds to the cancer drug imatinib with an inactive Abl/c-Kit conformation and a
1174 distributed thermodynamic penalty. *Structure*, 15(3), 299-311.
1175 doi:10.1016/j.str.2007.01.015
1176 Seeliger, M. A., Ranjitkar, P., Kasap, C., Shan, Y., Shaw, D. E., Shah, N. P., . . . Maly, D. J. (2009).
1177 Equally potent inhibition of c-Src and Abl by compounds that recognize inactive
1178 kinase conformations. *Cancer Res*, 69(6), 2384-2392. doi:10.1158/0008-5472.CAN-
1179 08-3953
1180 Shukla, D., Meng, Y., Roux, B., & Pande, V. S. (2014). Activation pathway of Src kinase reveals
1181 intermediate states as targets for drug design. *Nat Commun*, 5, 3397.
1182 doi:10.1038/ncomms4397
1183 Steeghs, N., Eskens, F. A. L. M., Gelderblom, H., Verweij, J., Nortier, J. W. R., Ouwerkerk, J., . . .
1184 de Jonge, M. J. A. (2009). Phase I Pharmacokinetic and Pharmacodynamic Study of
1185 the Aurora Kinase Inhibitor Danusertib in Patients With Advanced or Metastatic
1186 Solid Tumors. *Journal of Clinical Oncology*, 27(30), 5094-5101.
1187 doi:10.1200/Jco.2008.21.6655
1188 Taylor, S. S., Keshwani, M. M., Steichen, J. M., & Kornev, A. P. (2012). Evolution of the
1189 eukaryotic protein kinases as dynamic molecular switches. *Philosophical
1190 Transactions of the Royal Society B-Biological Sciences*, 367(1602), 2517-2528.
1191 doi:10.1098/rstb.2012.0054
1192 Treiber, D. K., & Shah, N. P. (2013). Ins and outs of kinase DFG motifs. *Chem Biol*, 20(6), 745-
1193 746. doi:10.1016/j.chembiol.2013.06.001
1194 Vajpai, N., Strauss, A., Fendrich, G., Cowan-Jacob, S. W., Manley, P. W., Grzesiek, S., & Jahnke,
1195 W. (2008). Solution conformations and dynamics of ABL kinase-inhibitor complexes
1196 determined by NMR substantiate the different binding modes of imatinib/nilotinib
1197 and dasatinib. *J Biol Chem*, 283(26), 18292-18302. doi:10.1074/jbc.M801337200
1198 Vogtherr, M., Saxena, K., Hoelder, S., Grimme, S., Betz, M., Schieberr, U., . . . Schwalbe, H.
1199 (2006). NMR characterization of kinase p38 dynamics in free and ligand-bound
1200 forms. *Angew Chem Int Ed Engl*, 45(6), 993-997. doi:10.1002/anie.200502770
1201 Willemsen-Seegers, N., Uitdehaag, J. C., Prinsen, M. B., de Vetter, J. R., de Man, J., Sawa, M., . . .
1202 Zaman, G. J. (2017). Compound Selectivity and Target Residence Time of Kinase
1203 Inhibitors Studied with Surface Plasmon Resonance. *J Mol Biol*, 429(4), 574-586.
1204 doi:10.1016/j.jmb.2016.12.019

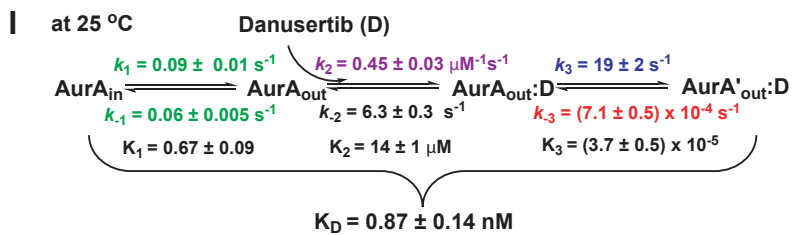
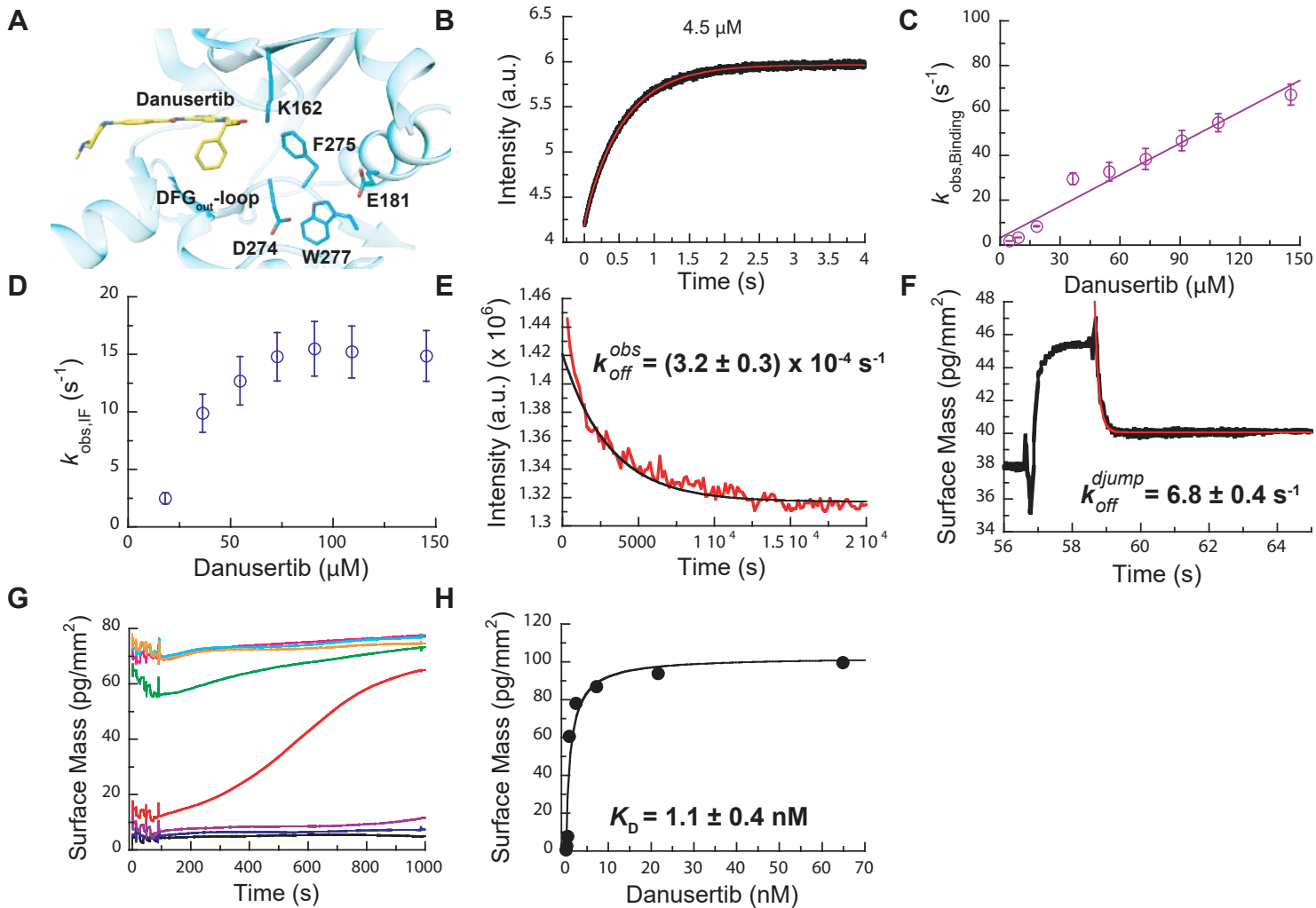
1205 Wilson, C., Agafonov, R. V., Hoemberger, M., Kutter, S., Zorba, A., Halpin, J., . . . Kern, D.
1206 (2015). Kinase dynamics. Using ancient protein kinases to unravel a modern cancer
1207 drug's mechanism. *Science*, 347(6224), 882-886. doi:10.1126/science.aaa1823
1208 Winn, M. D., Ballard, C. C., Cowtan, K. D., Dodson, E. J., Emsley, P., Evans, P. R., . . . Wilson, K.
1209 S. (2011). Overview of the CCP4 suite and current developments. *Acta Crystallogr D*
1210 *Biol Crystallogr*, 67(Pt 4), 235-242. doi:10.1107/S0907444910045749
1211 Winter, G. (2010). xia2: an expert system for macromolecular crystallography data
1212 reduction. *Journal of Applied Crystallography*, 43, 186-190.
1213 doi:10.1107/S0021889809045701
1214 Wojcik, J., Hantschel, O., Grebien, F., Kaupe, I., Bennett, K. L., Barkinge, J., . . . Koide, S. (2010).
1215 A potent and highly specific FN3 monobody inhibitor of the Abl SH2 domain. *Nat*
1216 *Struct Mol Biol*, 17(4), 519-527. doi:10.1038/nsmb.1793
1217 Wood, E. R., Truesdale, A. T., McDonald, O. B., Yuan, D., Hassell, A., Dickerson, S. H., . . .
1218 Shewchuk, L. (2004). A unique structure for epidermal growth factor receptor
1219 bound to GW572016 (Lapatinib): relationships among protein conformation,
1220 inhibitor off-rate, and receptor activity in tumor cells. *Cancer Res*, 64(18), 6652-
1221 6659. doi:10.1158/0008-5472.CAN-04-1168
1222 Xu, W., Harrison, S. C., & Eck, M. J. (1997). Three-dimensional structure of the tyrosine
1223 kinase c-Src. *Nature*, 385(6617), 595-602. doi:10.1038/385595a0
1224 Zhao, B., Smallwood, A., Yang, J., Koretke, K., Nurse, K., Calamari, A., . . . Lai, Z. (2008).
1225 Modulation of kinase-inhibitor interactions by auxiliary protein binding:
1226 crystallography studies on Aurora A interactions with VX-680 and with TPX2.
1227 *Protein Sci*, 17(10), 1791-1797. doi:10.1110/ps.036590.108
1228 Zheng, H., Cooper, D. R., Porebski, P. J., Shabalin, I. G., Handing, K. B., & Minor, W. (2017).
1229 CheckMyMetal: a macromolecular metal-binding validation tool. *Acta Crystallogr D*
1230 *Struct Biol*, 73(Pt 3), 223-233. doi:10.1107/S2059798317001061
1231 Zorba, A., Buosi, V., Kutter, S., Kern, N., Pontiggia, F., Cho, Y. J., & Kern, D. (2014). Molecular
1232 mechanism of Aurora A kinase autophosphorylation and its allosteric activation by
1233 TPX2. *Elife*, 3, e02667. doi:10.7554/eLife.02667
1234

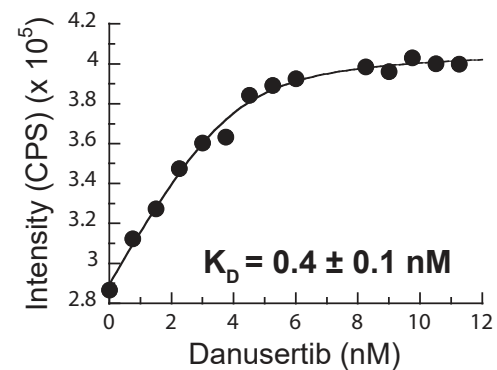
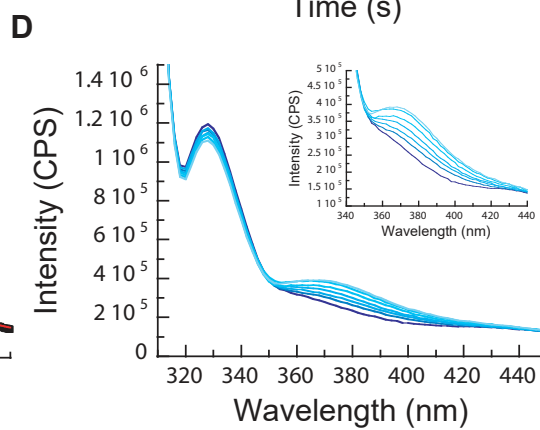
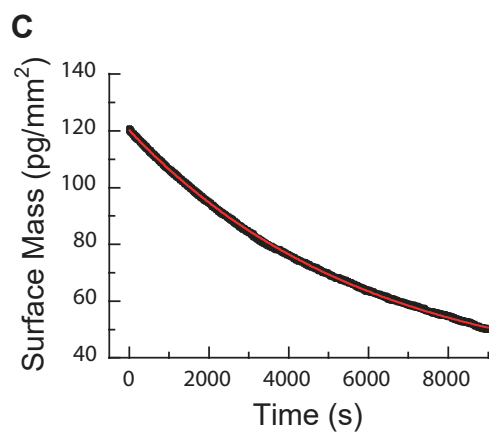
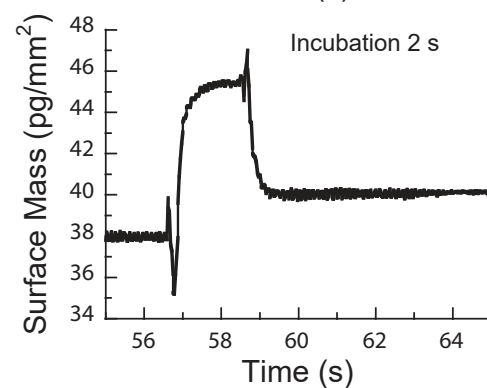
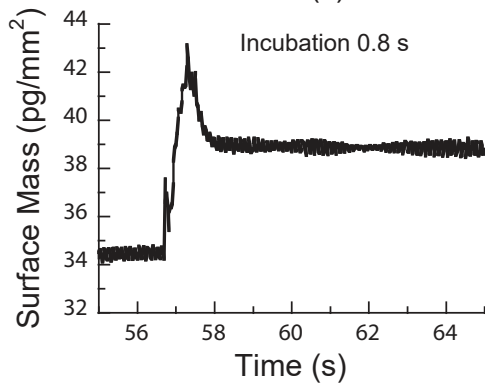
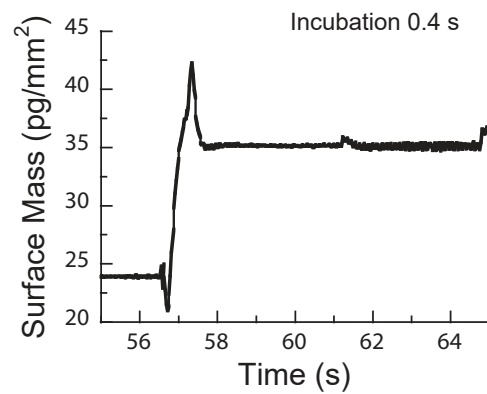
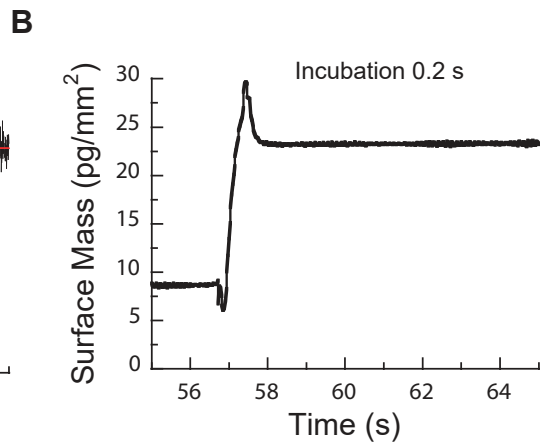
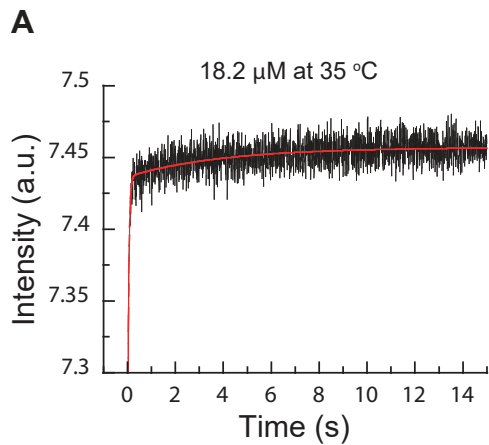


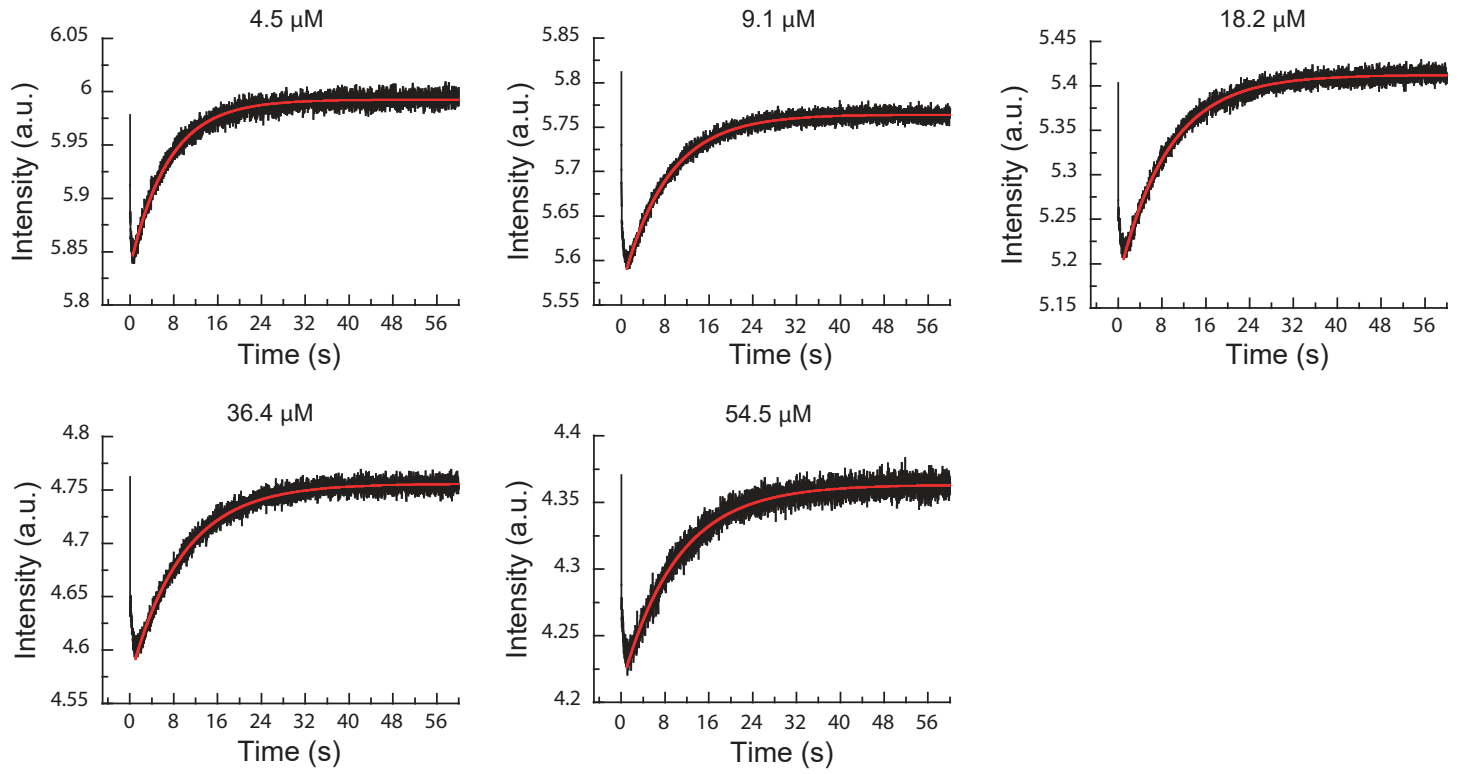
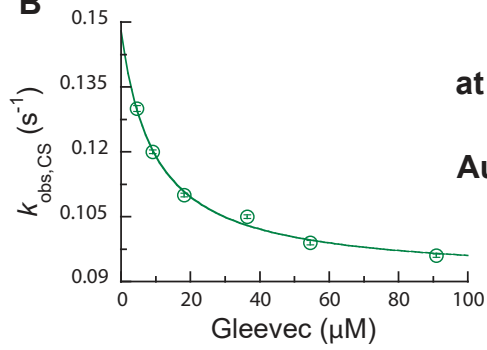
A**B****C****D**



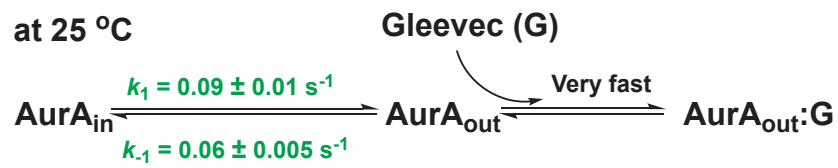


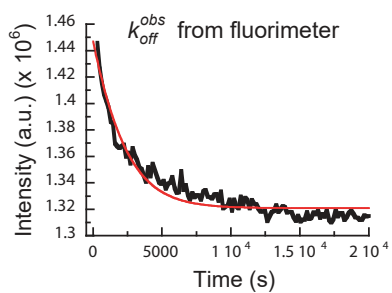
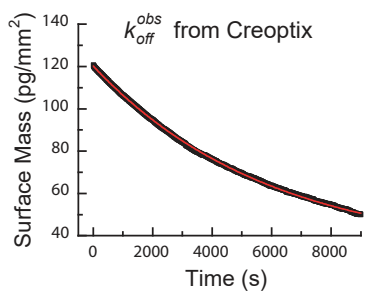
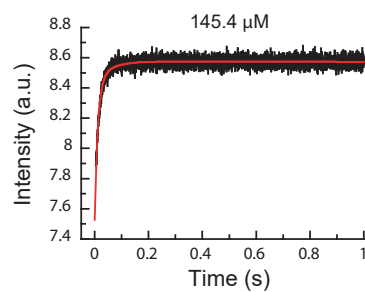
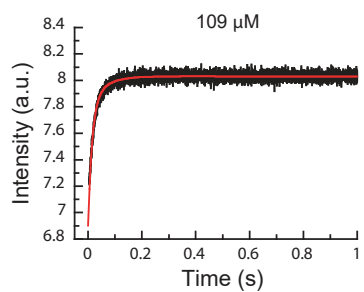
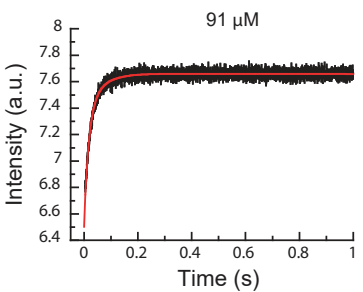
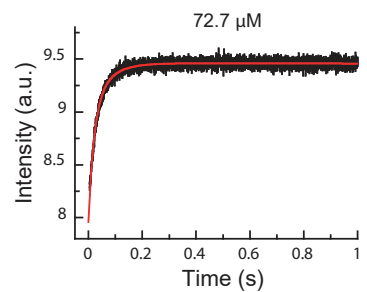
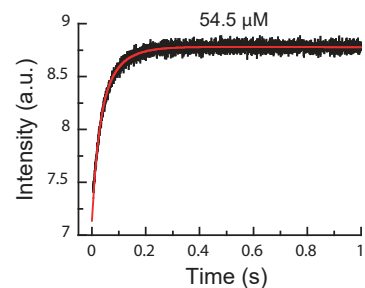
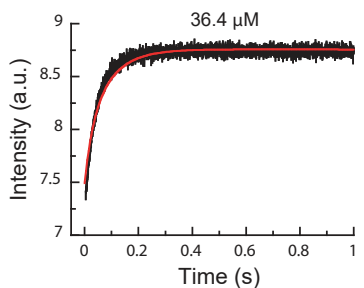
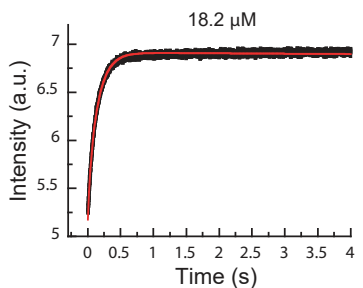
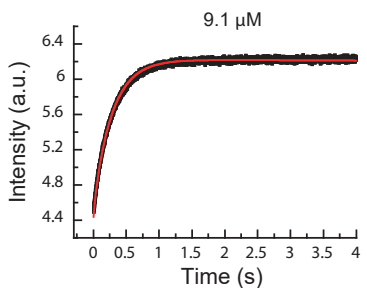
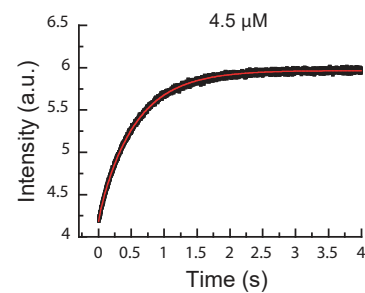
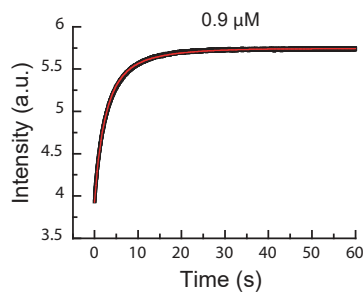
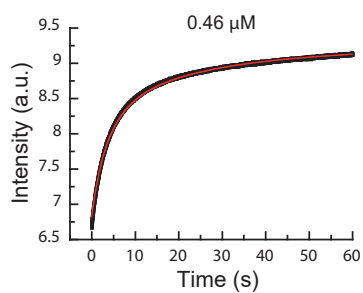
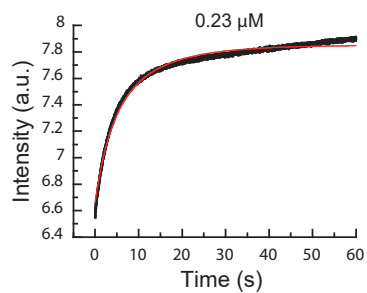




A**B**

at 25 °C

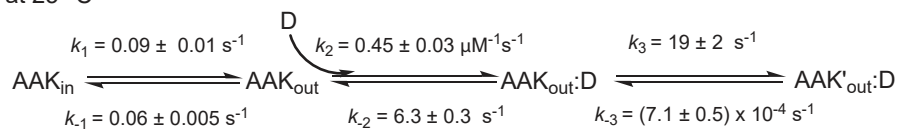




$$\text{Creoptix } k_{\text{slow-off}}^{\text{obs}} = (2 \pm 0.006) \times 10^{-4} \text{ s}^{-1}$$

$$\text{Fluorimeter } k_{\text{slow-off}}^{\text{obs}} = (3.2 \pm 0.3) \times 10^{-4} \text{ s}^{-1}$$

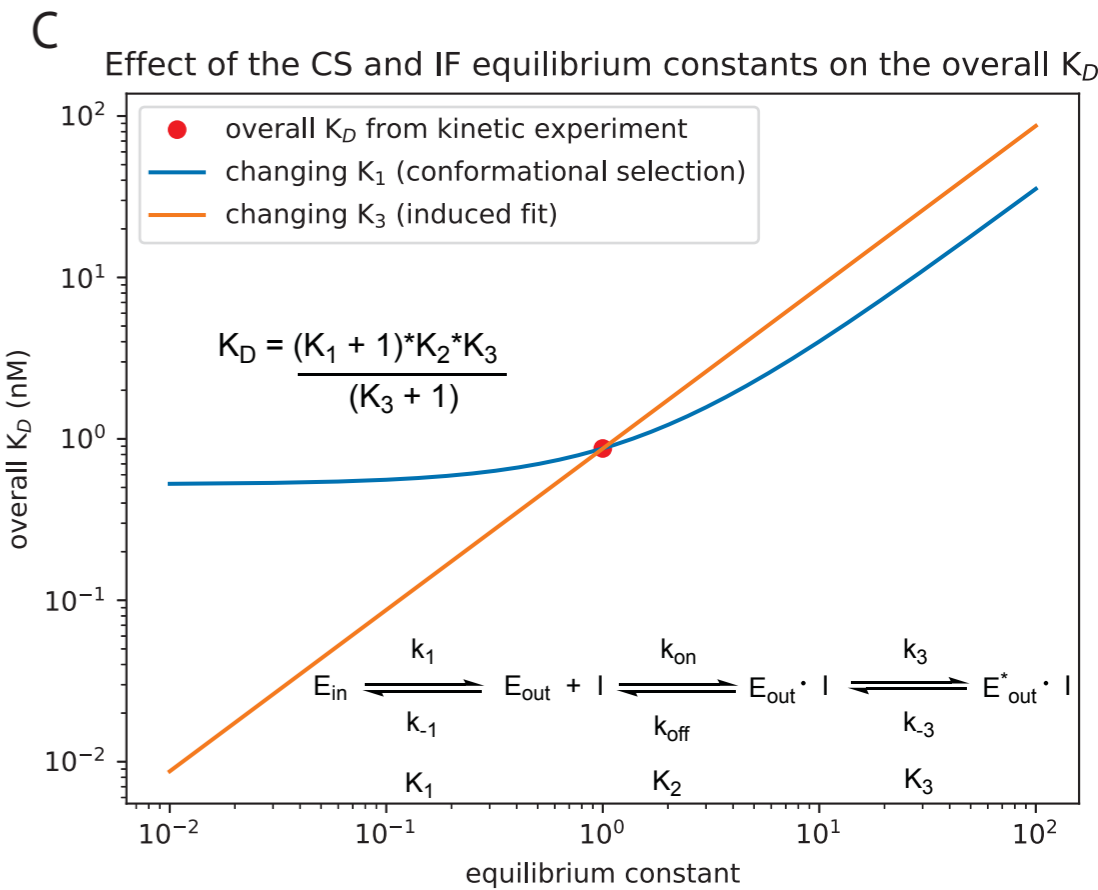
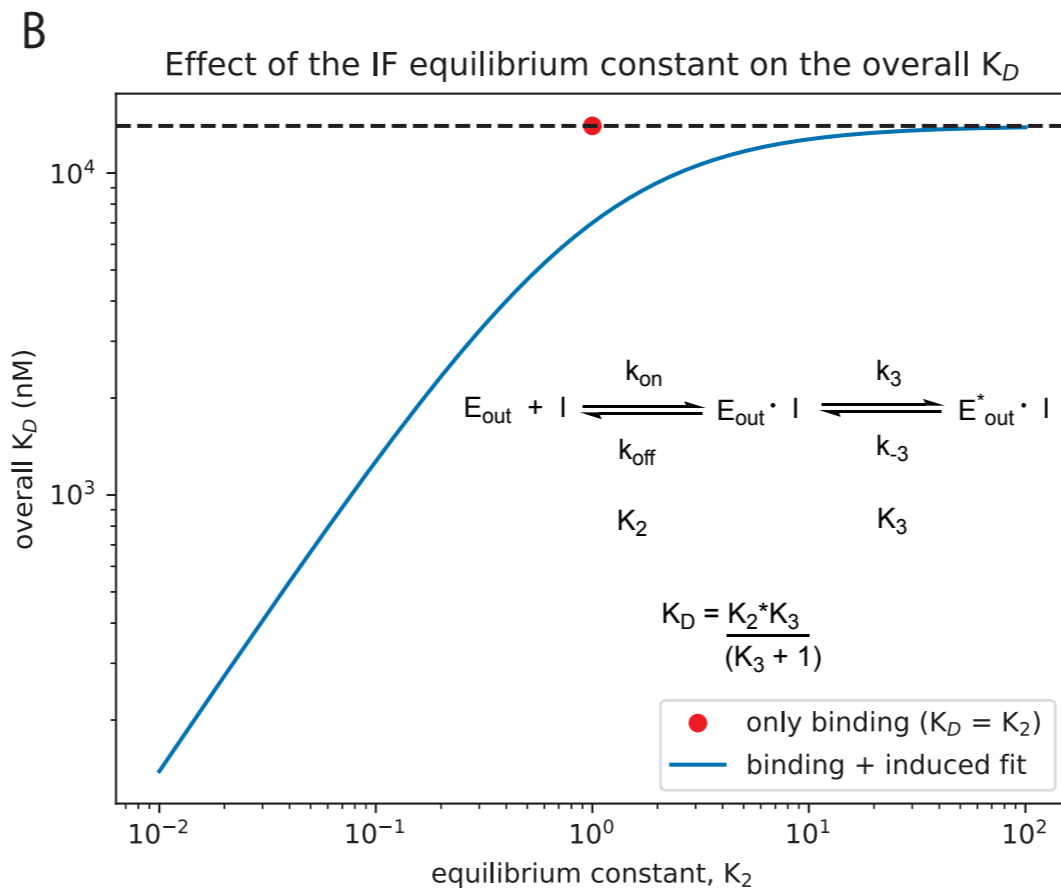
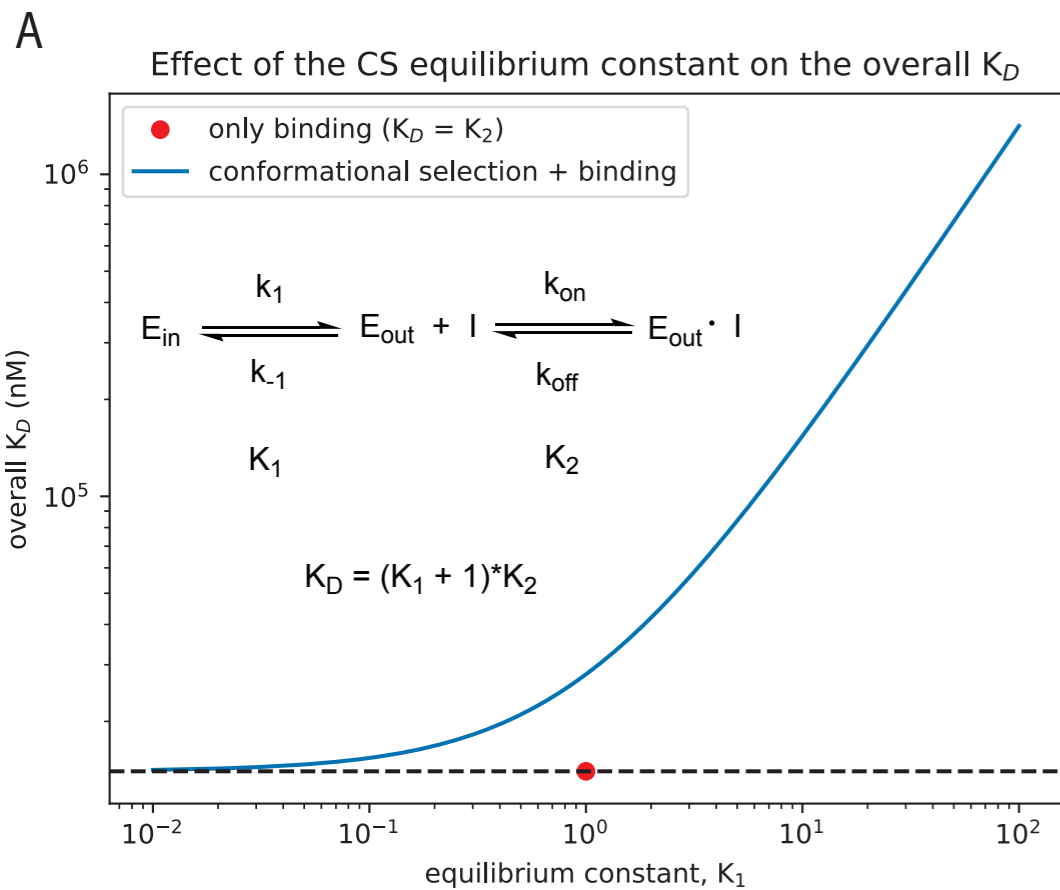
at 25 °C

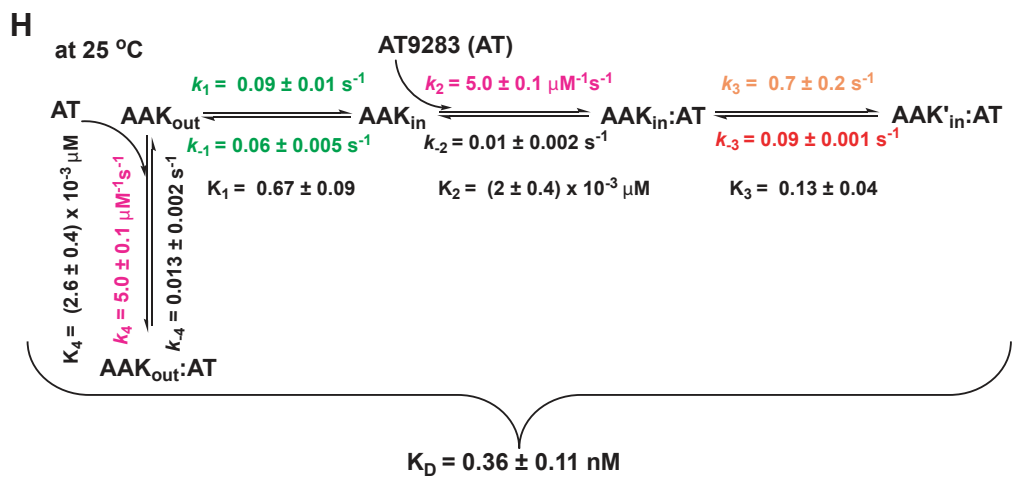
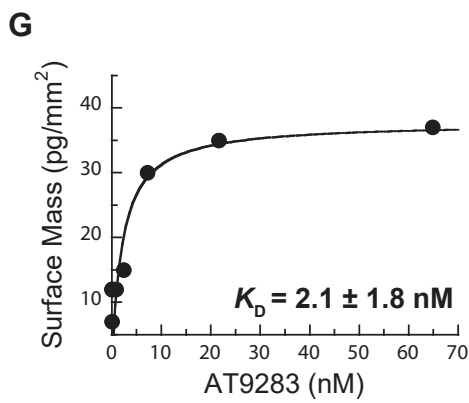
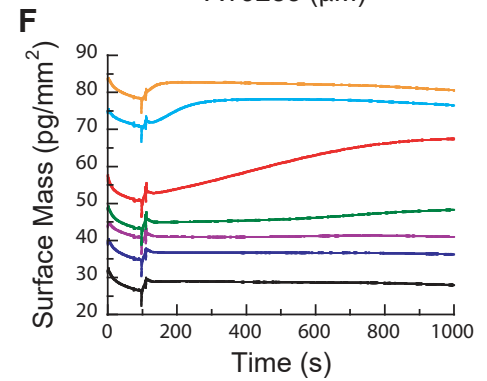
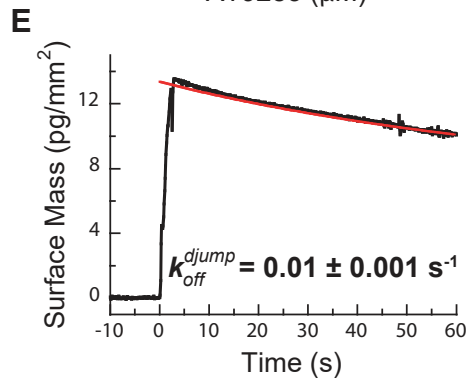
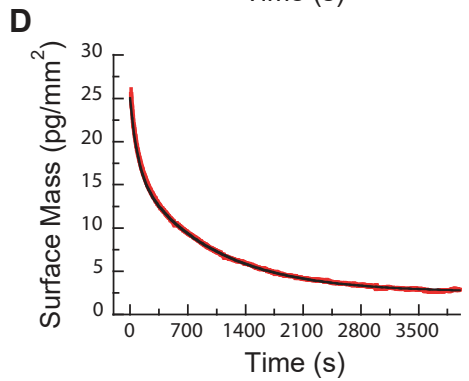
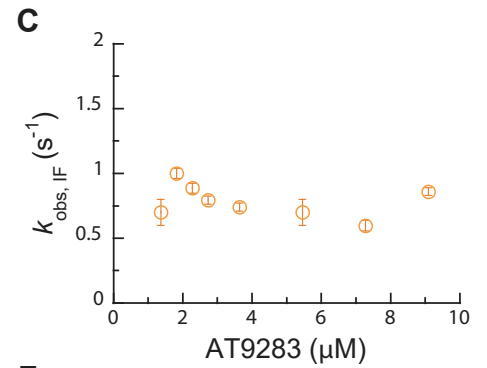
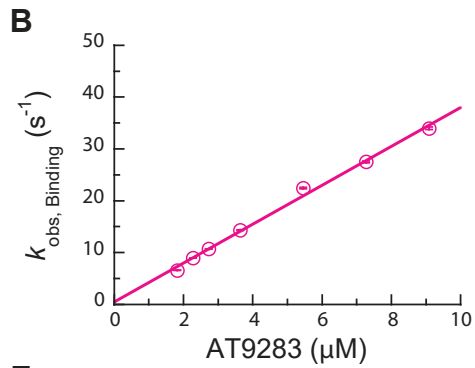
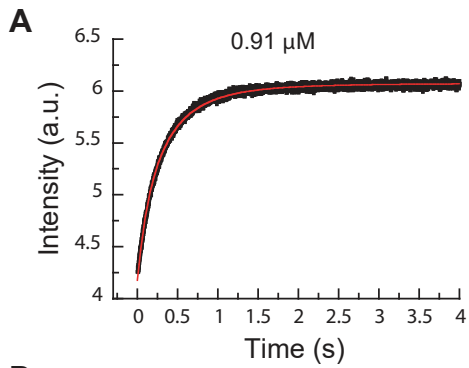


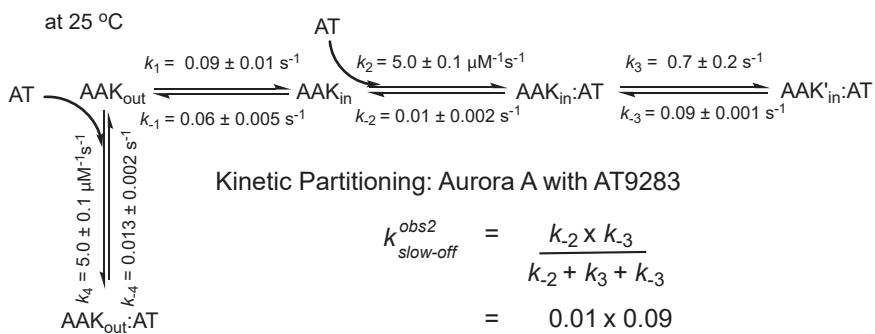
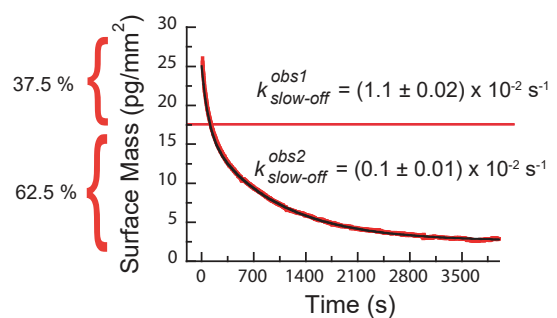
Kinetic Partitioning: Aurora A with Danusertib

$$\begin{aligned}
 k_{\text{slow-off}}^{\text{obs}} &= \frac{k_{-2} \times k_{-3}}{k_{-2} + k_3 + k_{-3}} \\
 &= \frac{6.3 \times (7.1 \times 10^{-4})}{6.3 + 19 + (7.1 \times 10^{-4})}
 \end{aligned}$$

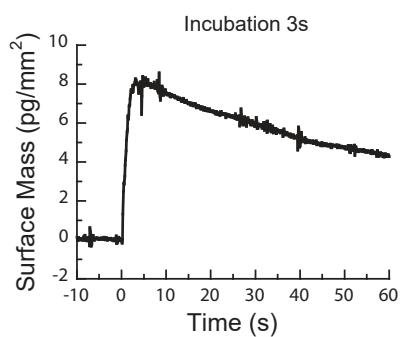
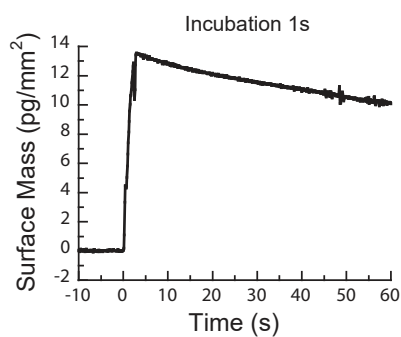
$$k_{\text{slow-off}}^{\text{obs}} = (1.77 \pm 0.2) \times 10^{-4} \text{ s}^{-1}$$

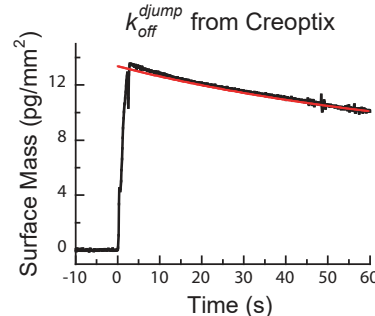
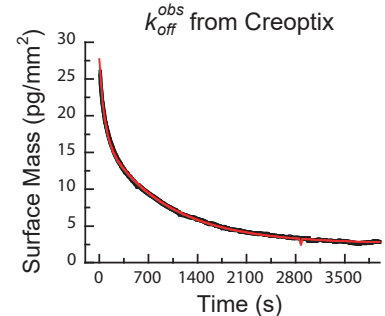
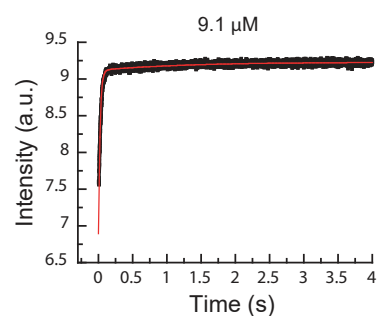
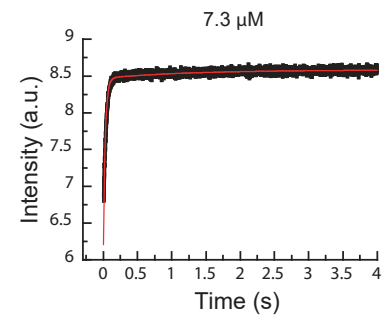
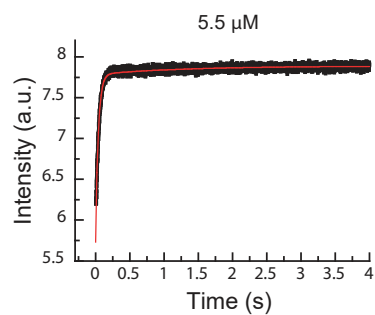
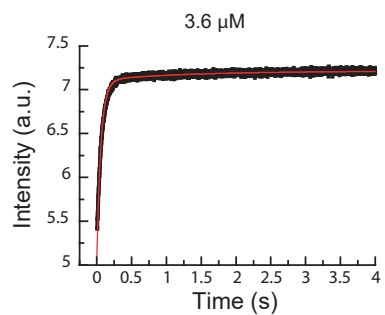
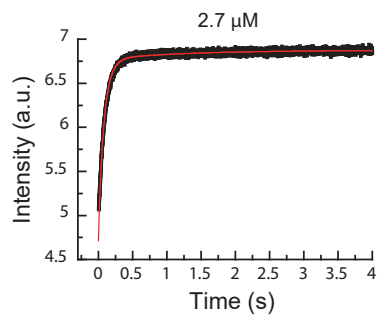
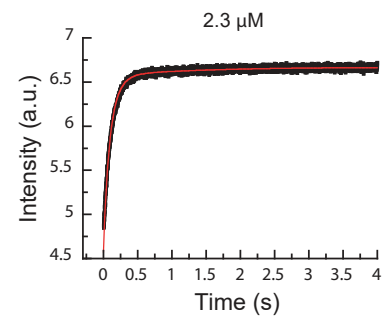
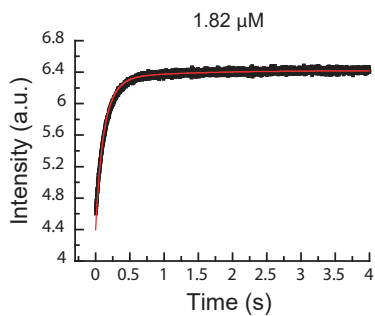
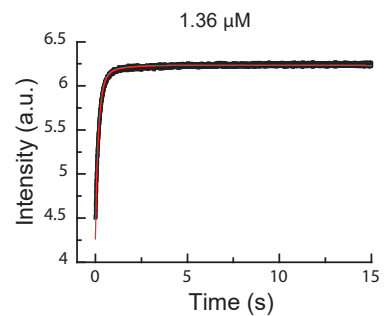
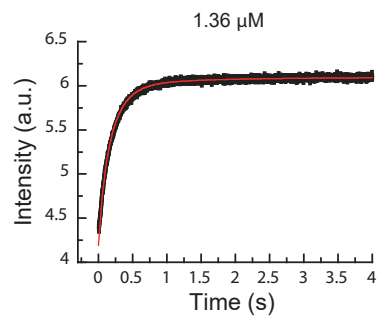
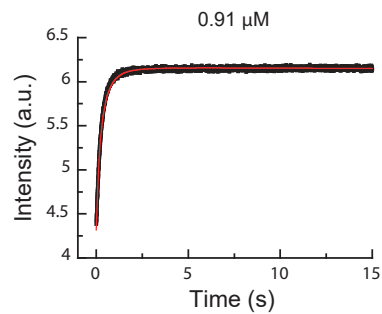
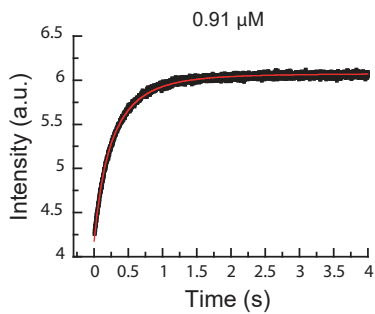
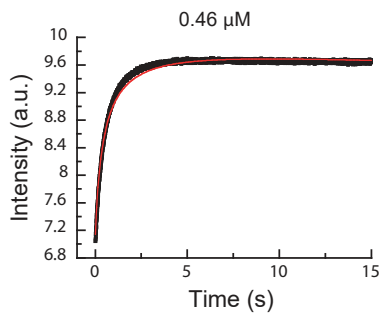
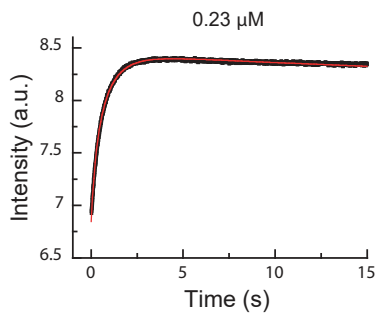


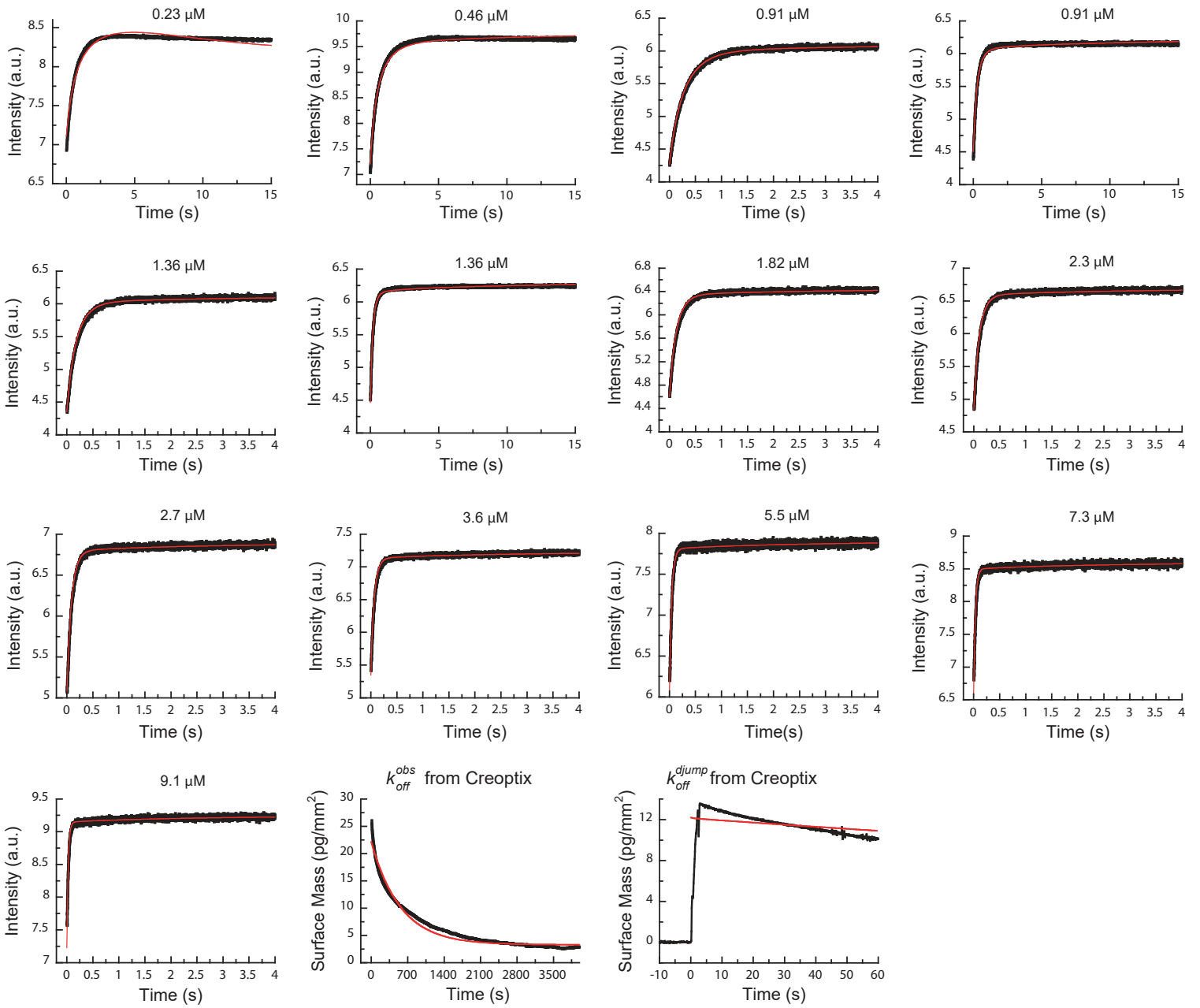
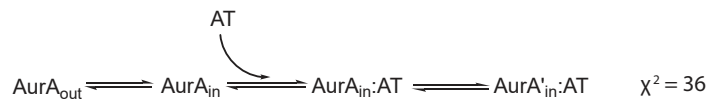
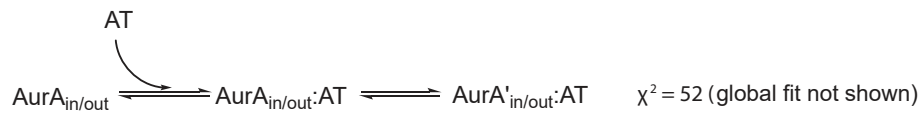


A

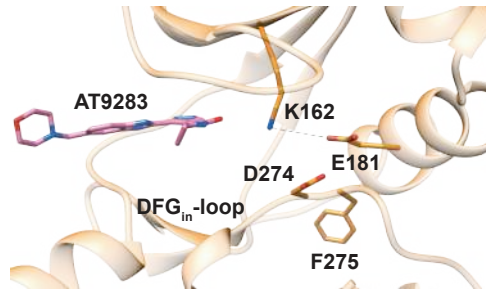
$$\begin{aligned}
 k_{slow-off}^{obs2} &= \frac{k_2 \times k_3}{k_2 + k_3 + k_4} \\
 &= \frac{0.01 \times 0.09}{0.01 + 0.09 + 0.7} \\
 k_{slow-off}^{obs2} &= (1.1 \pm 0.4) \times 10^{-3} \text{ s}^{-1}
 \end{aligned}$$

B



A**B**

A



B

